Pantasma: evidence for a Pleistocene circa 14 km diameter impact crater in Nicaragua

Pierre Rochette, R. Alaç, P. Beck, G. Y. Brocard, A. J Cavosie, V. Debaille, Bertrand Devouard, F. Jourdan, B. Mougel, F. Moustard, et al.

Pantasma: evidence for a Pleistocene circa 14 km diameter impact crater in Nicaragua

P. Rochette[1], R. Alaç [2], P. Beck[3] , G. Brocard[2], A. J. Cavosie[4], V. Debaille[5] , B. Devouard[1] , F. Jourdan[4], B. Mougel[6*], F. Moustard[1], F. Moynier[6], S. Nomade[7], G. R. Osinski[8] , B. Reynard[9] and J. Cornec[10]

[1] Aix-Marseille Univ., CNRS, INRA, IRD, Coll. France, CEREGE, 13545 Aix-en-Provence, France, [2] Earthbyte Group, School of Geosciences, University of Sydney, Australia, [3] IPAG Grenoble, France, [4] Space Science and Technology Centre and The Institute for Geoscience Research (TIGeR), School of Earth and Planetary Science, Curtin University, Perth, Western Australia, Australia, [5] Laboratoire G-Time, Université Libre de Bruxelles, Brussels, Belgium, [6] Institut de Physique du Globe de Paris, Université Sorbonne Paris Cité, CNRS UMR 7154, Paris, France [7] LSCE, Gif sur Yvette, France, [8] Centre for Planetary Science and Exploration, Department of Earth Science, University of Western Ontario, London, Canada, [9] Laboratoire de Geologie de Lyon, CNRS UMR 5276, Ecole Normale Supérieure de Lyon, France [10]Denver, USA.
*now at Centro de geociencias, Universidad Nacional Autónoma de México, Campus Juriquilla, Querétaro
E-mail: rochette@cerege.f

Abstract

The circa 14 km diameter Pantasma circular structure in Oligocene volcanic rocks in Nicaragua is here studied for the first time to understand its origin. Geomorphology, field mapping, petrographic and geochemical investigations all are consistent with an impact origin for the Pantasma structure. Observations supporting an impact origin include outward-dipping volcanic flows, the presence of former melt-bearing polymict breccia, impact glass (with lechatelierite and low H_2O, < 300 ppm), and also a possible ejecta layer containing Paleozoic rocks which originated from hundreds of meters below the surface. Diagnostic evidence for impact is provided by detection in impact glass of the former presence of reidite in granular zircon as well as coesite, and extra-terrestrial $\varepsilon^{54}Cr$ value in polymict breccia. Two $^{40}Ar/^{39}Ar$ plateau ages with a combined weighted mean age of 815 ± 11 ka (2 σ; P=0.17) were obtained on impact glass. This age is consistent with geomorphological data and erosion modeling, which all suggest a rather young crater. Pantasma is only the fourth exposed crater > 10 km found in the Americas

south of N30 latitude, and provides further evidence that a significant number of impact craters may remain to be discovered in Central and South America.

INTRODUCTION

Impact cratering constitutes a major process in the evolution of solid bodies in the solar system, as testified by a $\sim 10^6$ crater count for Mars and the Moon (see Robbins and Hynek, 2012; Robbins 2018). The 190 impact craters identified on Earth as of 2018 are of paramount importance to the understanding of the cratering process. Only on Earth can the same impact structure be studied from the micrometer to kilometer scale with all techniques available in the laboratory or in the field, with emphasis for example on impact metamorphism, ejecta or impactor characteristics (e.g., Folco et al., 2011). The vertical dimension is of particular interest given its limited accessibility on other solar system bodies. This dimension is accessible on Earth as a consequence of erosion (Osinski and Ferrière 2016), drilling (e.g., Koeberl et al., 2007a) as well as geophysical methods (Pilkington and Grieve, 1992). Based on the significant scientific findings made in newly discovered craters (e.g., Folco et al., 2011; Osinski and Ferrière 2016), discovery of new craters continues to improve our knowledge of the cratering process and the Earth's cratering record.

The limited terrestrial cratering record provides motivation to search for new impact structures, as advocated for Africa by Reimold and Koeberl (2014) and for Brazil by Crosta and Vasconcelos (2013). Impact structure identification in Central and South America is hampered by various factors, including limited field studies, heavily vegetated inter-tropical areas, and by complex and young geomorphology mainly due to the active volcanism linked to the panamerican subduction zone. We investigate here a large circular structure from Nicaragua in Central America named Pantasma, first

mentioned by Kowald (2006) based on satellite imagery. A previous investigation considered the Pantasma structure as a possible source for tektite-like glass from the Belize impact glass field (Povenmire et al., 2011), which has been dated at 777 ± 32 ka (2σ; Schwarz et al., 2016). Candidate impact structures detected by remote sensing such as Pantasma need to be investigated on the ground in order to collect diagnostic evidence for impact, as outlined by French and Koeberl (2010) and Reimold and Koeberl (2014).

GEOLOGICAL CONTEXT

The circular Pantasma structure is centered at 13°22'N and 85°57'W in the volcanic Nicaragua Highlands (Fig. 1a). It consists of a well-defined circular depression ~400 m above sea level that is surrounded by steep hills that rise 100 to 600 m higher than the depression (Fig. 1b). The official name of the depression on the 1:50,000 topographic map of Nicaragua is "Valle di Santa Maria di Pantasma", which is here shortened to "Pantasma". A regional northward slope is visible in the rim crest, as well as in the general drainage pattern. The whole structure is strongly dissected by the Pantasma River, which flows through the depression from south to north.

General geological maps of the area (Fig. 1a, Ehrenborg, 1996; Arengi and Hodgson, 2000; Elming et al., 2001) show that the structure formed in Oligocene volcanic flows of the Matagalpa Group, which is estimated to range from 0.3 to > 1.5 km thick and is dated to between 25 and 32 Ma (Elming et al., 2001). Bedrock compositions range from andesite to rhyolite, and lithologies include lava flows and ignimbrites (welded tuffs, volcanoclastic layers) interbedded with fluvial sediments, including rare occurrence of obsidian (Mrazova and Gadas, 2011). The overlying Miocene to early Pleistocene age (based on map relations) Coyol Group contains more basaltic flows and

is exposed south of the Pantasma structure (Fig. 1a). The upper Coyol Group is assumed to be Pleistocene, although the most recent synthesis places its upper boundary near 7 Ma (Saginor et al., 2011). Basement underlying the Tertiary volcanics consists of Paleozoic schist, with the nearest exposures located ~15 km north of the structure. A few Tertiary and older intrusions also outcrop in the area (Fig. 1a). Of significance to this study, no post-Miocene volcanic activity has been documented in the area (Saginor et al., 2011). The closest Quaternary volcanic centers are restricted to the Nicaraguan Depression, located ~100 km southwest of the Pantasma structure.

SAMPLES AND METHODS

Quantitative analysis of topography was performed using Shuttle Radar Topographic Mission (SRTM) 90 m digital elevation model (DEM) treated with ArcGIS and QGIS software. Fieldwork was conducted in January 2016 for 5 days, and included systematic mapping of the structure as well as collection of rock and soil samples (listed in suppl. Table A).

Major and trace element analyses were performed at the Laboratoire G-Time at the Université Libre de Bruxelles. For each sample, approximately 50 mg of crushed material was dissolved by alkaline fusion using ultrapure (>99.999%) lithium metaborate. Major elements were measured using a Thermoscientific ICaP inductively-coupled plasma atomic emission spectroscopy (ICP-AES) instrument. International standards BCR-2, BHVO-2, AGV-2 and BIR-1 were used for monitoring accuracy. The relative difference between the accepted and measured values was lower than 5% for individual elements and lower than 2% for the total wt. %. Loss on ignition (LOI) was measured after 1 hour at 1000°C and corrected for Fe content. For trace elements, the concentrations were measured on an Agilent 7700 quadrupole ICP-mass spectrometer.

External reproducibility based on natural duplicate analyses is generally lower than 10% (2 relative standard deviation RSD), except for Cr, Ni and Cu (< 20% 2 RSD). International standards BCR-2, AGV-2 and BHVO-2 were used to monitor accuracy and yielded results within the accepted range.

Thin sections of representative rocks were prepared for optical microscopy, while polished thick sections of the glass were examined in CEREGE using a Hitachi S3000-N scanning electronic microscope (SEM) fitted with a Bruker energy dispersive spectrometry (EDS) microanalysis system, using a 15 kV voltage. Further microanalyses were obtained by electron microprobe analysis using a CAMECA SX-100 at the Centre de Microanalyse de Paris VI (CAMPARIS). Polished thin sections of breccia were also analyzed on a JEOL JXA 8530F hyperprobe in the Earth and Planetary Materials Analysis Laboratory at the University of Western Ontario.

Electron backscatter diffraction (EBSD) analysis of two zircons in glass sample P2 was done using a Tescan MIRA3 field emission gun (FEG) SEM in the Microscopy and Microanalysis Facility at Curtin University. Orientation maps were collected using step sizes of 180 nm (whole-grain) and 150 nm (regions of interest). EBSD analyses used a 20 kV accelerating voltage, 70° sample tilt, 20.5 mm working distance, and 18 nA beam intensity (further details in supplementary material).

Double-polished sections were prepared from three glass samples in order to determine water content through transmission measurements. Samples were polished using SiC disks under ethanol until they were optically thin through the spectral range of interest and their thickness was measured using a Mitutoyo Digimatic micrometer. Water content was determined using Fourier transform infra-red (FTIR) transmission microscopy with a VERTEX V70 spectrometer coupled to a Hyperion 3000 infrared microscope (IPAG, Grenoble; further details in supplementary material).

Raman spectra of SiO_2 rich inclusions in the glass were obtained using a LabRAM HR800 Evolution spectrometer that has a confocal Czerny-Turner geometry and a laser source of 532 nm in wavelength. Each spectrum was acquired with a power of 10 mW, and 25 accumulations of 5 to 15s. Gratings with 600 groove/mm were used in order to cover the frequency range 60 to 1300 cm^{-1}.

For Ar/Ar geochronology, glass fragments were hand-picked from the 215-315 μm fraction of glass sample P2 under the binocular stereomicroscope and were thoroughly rinsed in distilled water and loaded into an aluminium disc. The glass sample was irradiated for 3 hours alongside FCs standards (Jourdan and Renne, 2007), for which an age of 28.294 Ma (± 0.13%) was used (Renne et al., 2011). The discs were Cd-shielded (to minimize undesirable nuclear interference reactions) and irradiated in the Oregon State University nuclear reactor (USA) in central position. The $^{40}Ar/^{39}Ar$ analyses were performed at the Western Australian Argon Isotope Facility at Curtin University. Three aliquots of glass with weight ranging from about 10 to 40 mg were step-heated using a continuous 100 W PhotonMachine© CO_2 (IR, 10.4 μm) laser fired on the glass during 60 seconds per step. Each of the standard crystals was fused in a single step. The gas was purified in an extra low-volume stainless steel extraction line of 240cc and using one SAES AP10 and one GP50 getter. Ar isotopes were measured in static mode using a low volume (600 cc) ARGUS VI mass spectrometer from Thermofisher© set with a permanent resolution of ~200 (further details in supplementary material).

For Cr isotope analysis, 30 mg of breccia sample P5B was dissolved in a 3:1 mixing of HF-HNO_3 in Teflon bombs at 140°C. The chemical separation was adapted from Trinquier et al. (2008) and described in detail in Mougel et al. (2018). It includes three separation steps of Cr on cationic exchange resin AG50W-X8 and was conducted at the Institut de Physique du Globe de Paris. $^{53}Cr/^{52}Cr$ and $^{54}Cr/^{52}Cr$ isotope ratios were

measured by Thermal-Ionization Mass-Spectrometry (TIMS) Fisher Scientific Triton at the Center for Star and Planet Formation, University of Copenhagen using a filament exhaustion sample standard bracketing approach following the method described in Van Kooten et al. (2016). Chromium isotopic data are reported using the ε -unit, which represents the relative deviation in parts per 10,000 of $^{53}Cr/^{52}Cr$ and $^{54}Cr/^{52}Cr$ ratios from a terrestrial standard (NIST SRM 3112a Cr standard; see supl. Table B). In addition to breccia sample P5B, a USGS geostandard, BHVO-2, was analyzed during the same session to check for the accuracy of the method.

Magnetic susceptibility (χ) measurements of glass samples P1 to P4 were performed using a MFK1 Kappabridge, at two frequencies F1=0.98 and F3=15.6 kHz. Reported values are at F1 frequency and we computed the frequency dependence as $fd\% = (\chi_{F1}-\chi_{F3})/\chi_{F1} \times 100$. Susceptibility versus temperature curves were obtained by heating under Argon flow using the CS3 attachment. Hysteresis cycles were obtained on a Micromag vibrating sample magnetometer (VSM) with maximum field of 1 Tesla. High-field susceptibility (χ_{hf} of mostly paramagnetic origin) was computed from the above 0.7 T part of the cycle. Note that low field susceptibility was measured on samples of several grams while hysteresis was measured on samples up to a few 100 mg in size. Natural remanence (NRM) and anhysteretic remanence (ARM, acquired in 120 mT AF field and 0.2 mT bias field) were demagnetized and measured using a 2G superconducting remanence magnetometer. All magnetic measurements were conducted at CEREGE. We also performed bulk density determinations using helium pycnometry with a Quantachrome instrument.

RESULTS

Field observations

The region around the Pantasma structure is densely populated, and the hills surrounding the depression are heavily forested. The depression itself, where the municipality of Las Praderas sits along the Pantasma River, is characterized by agricultural fields. Outcrops are found mostly along road cuts, in a few small quarries, and in riverbeds. Due to pervasive tropical weathering and active soil formation, most road cuts expose surface formations and where available, rocky outcrops are often hard to interpret due to weathering. Fresh rocks were only found as gravel and boulders in river beds and in a single large outcrop, exposed on the highest hill of the south rim at a hydroelectric plant ("Torre de Oscilacion"; TO in Fig.1b). Outcrops are rare outside the structure and more or less absent within the depression. Effort was devoted to obtain bedding measurements, however, not all volcanic outcrops allowed the accurate determination of bedding attitude due to limited surface area, weathering, massive texture or fracturing.

Outcrops from the depression rim, or further outside the structure, essentially consist of volcanic formations, and in one instance, interbedded conglomeratic sediments. The formations look like massive flows with interbedded pumice layers. The relatively acidic compositions, as confirmed by thin section and geochemical analysis (see below), are consistent with these rocks belonging to the Matagalpa Group (e.g. Ehrenborg, 1996). Apart from the TO site, outcrops show constant tilt. The bedding map (Fig. 1b) shows a general circular symmetry dipping outward, except in one site, and decreasing dip away from the rim. One quarry (Q in Fig. 1b) with an inward dip shows a continuum between highly fractured concordant beds and a monomict megabreccia of the same material, that is injected with white veins. The TO site, with continuous outcrop over 30 m high and several hundred meters long is an exception; it shows zones of horizontal and vertical bedding. The contact between the two appears to be fault

gouge (Fig. 2b). In another part a steep recumbent fold is visible (Fig. 2a). Fracturing is pervasive but no convincing shatter cones (SC) were observed.

Moving down the rim towards the center of the depression we observed a few breccia outcrops, as well as the presence of up to meter-sized breccia blocks in fields and rivers. The breccia is polymict, containing volcanic clasts from millimeter to meter in size, within a whitish matrix. Its appearance strongly resembles impact breccia (e.g., Dressler and Reimold, 2001), although field observations cannot rule out a volcanoclastic origin. Within the depression, boulders of breccia (Fig. 2c; samples labeled P5) are abundant in the Pantasma River, downstream of the main Las Praderas breccia outcrop, unfortunately not reachable because of river entrenchment. This suggests that the main source of breccia is likely within the depression.

Of special significance is an outward dipping layered outcrop of unconsolidated material on the north rim containing angular centimeter-size clasts of Paleozoic schist and fractured quartz, with rare clasts of Matagalpa Group volcanics, overlying a faulted volcanic layer (suppl. Fig. A; star on Fig.1b). It is suggestive of an impact ejecta layer, produced by excavating Paleozoic basement from likely a few hundred meters below the surface and mixing it with the Matagalpa volcanics.

Inside the depression outcrops are rare and most are recent horizontal beds of fluviatile sand and conglomerate. Just below the main church at Las Praderas, a road-cut exposes a 10 m thick horizontal sequence of fine-layered sediments that appear to be lacustrine in origin. This sequence overlies the main breccia outcrop. In the same area we found on the river banks four pebble-size pieces of black glass (P1 to P4; Fig. 2d). While P1 to P3 are more or less layered compact glass, with masses from 3.6 to 64 g, P4 is a larger angular fractured cobble (circa 200 g) with a clear perlitic structure. Obsidian gravels were described by Mrazova et al. (2011) in a river 40 km south of Pantasma,

derived from local outcrops of Matagalpa Group ignimbrites. We note that only two other occurrences of obsidian have been described in Nicaragua, despite intensive investigation by archeologists (see review in Aggen 2007). These occurrences (toward the south of the site described in Mrazova et al. 2011) correspond to a few loose gravels recovered. Overall, obsidian appears to be rare in Matagalpa Group volcanic rocks.

Petrography and magnetic properties of glass samples

Optical and BSE imagery shows that glass samples P1-P3 are flow-textured and heterogeneous at different scales (Figs. 3a, c). Inclusions are numerous, including scoriaceous Si-rich clasts (Figs. 3c, d), and nearly pure SiO_2 zones typical of lechatelierite. The latter, in the 50-500 μm size range, are often elongated and twisted, forming rounded and diffuse boundaries with the surrounding host glass. Their chemical composition was first determined by EDS (the only elements detected were Si and O) and was later confirmed by electron microprobe analysis on several samples (all analyses with SiO_2> wt. 96%). SiO_2 content of the inclusion shown in Figure 3f is 99.6±0.2 wt.% (based on 5 spot analyses and totals normalized to 100%). While P2 and P3 are mostly pure translucent glass, P1 shows bands of more opaque material (suppl. Fig.B). In these bands, unmelted grains (iron oxide, amphibole and quartz), partially recrystallized glass, as well as a brecciated texture are observed (Fig.4). Raman spectra were collected on a thick section of sample P1. Five silica clasts were studied, of which typical spectra are shown (Fig. 5). Three clasts have typical spectra of coesite along with minor lechatelierite (Sharma et al. 1981), in proportions that vary slightly within the clasts. Coesite appears polycrystalline (micrometric grain size) under the optical microscope. One clast has typical spectra of lechatelierite with minor contribution from minute coesite grains. One clast displays typical spectra of quartz and polycrystalline

texture on its rims, and an optically homogeneous center with shocked quartz and lechatelierite. Recrystallized quartz at clast rim has its major peak at 464 cm^{-1} as expected, while shocked quartz in the clast center has its major peak at 461 cm^{-1}, and other peaks are also shifted to lower wavenumbers (McMillan et al. 1992). This texture is interpreted as recrystallization of shocked clast rims in the impact melt.

Two granular neoblastic zircon grains were identified in glass sample P2 (Fig. 6a). The zircon grains consist of μm-sized neoblasts, many of which contain ZrO_2 inclusions (Fig.6b-d). Orientation mapping by EBSD (Fig. 7a,b) reveals that neoblasts in each grain form three orientation clusters that are mutually orthogonal, as evidence by the coincidence of poles for (001) and {110}. These orientations only form in zircon that first transformed to reidite, and then back-transformed to zircon, leaving high-angle misorientations that can be ascribed to either reidite formation (90°/<110>), or {112} twin formation (65°/<110>) (Cavosie et al., 2016, 2018a and b; Erickson et al., 2017; Timms et al., 2017). High-angle misorientation plots (Fig. 7c) provide further evidence for the former presence of both {112} twins and reidite. Orientation data for the second granular zircon from glass sample P2 is similar to that shown in Figure 7, and is presented in Cavosie et al. (2018b).

Iron oxides occur in increasing abundance from glass sample P3 to P1 (in accordance with magnetic measurements) with a clear distinction between μm-sized particles (Fig. 8a-c) and patches larger than 10 μm. In glass sample P2 these patches have textures suggestive of liquid droplets intermingled with the silicate liquid, with subsequent dendritic growth in some cases (Fig. 8b).

EDS results on 15 oxide grains from glass sample P2 reveal that their cationic formula ($Fe_{3-x}\ M_x\ O_4$) is homogeneous within a grain but quite variable from grain to grain, with x from 0.18 to 1 (average 0.48) and average M being $Ti_{0.19}\ Al_{0.14}\ Mg_{0.12}\ Mn_{0.02}$.

Further microprobe analyses on 7 grains from the same section (2 points per grain, see suppl. Table D) yield x from 0.14 to 0.71 (average 0.50) with average M being $Ti_{0.28}$ $Al_{0.09}$ $Mg_{0.06}$ $Mn_{0.05}$ $V_{0.01}$. We refer to these objects as "granular magnetite". The less dense material that separates the oxide lobes is SiO_2-rich. Even if areas with the least content of µm-sized less dense inclusions were selected for EDS analyses, SiO_2 between 0.6 and 2.6 (average 1.2) wt.% were measured but we assumed that Si is outside the oxide structure.

In contrast to glass samples P1-P3, SEM examination of perlitic glass sample P4 reveals features more characteristic of volcanic glass, including primary crystals of amphibole, plagioclase, ilmenite, apatite, as well as inclusions of finely crystallized volcanic rocks (suppl. Fig. C).

Bulk density measurements on P1 and P2 yields values of 2.46 and 2.55 g/cm^3 kg/m^3, in agreement with a higher vesicularity of P1. Magnetic susceptibility (χ) of the four glass samples varies from 0.37 to 25.6 10^{-6} m^3/kg. Values are quite variable for different fragments. Hysteresis measurements confirm a variable saturation magnetization (M_s) and parameters typical of fine-grained magnetite (Table 1). This is consistent with a highly variable magnetite content (from to 0.1 to 2.0 %), typical of both oxidized impact glasses (e.g. Wabar, Irghizite, Atacamaite) and obsidian (Rochette et al. 2015). Domain state is pseudo-single domain for glass samples P1 and P3 plus one sub-sample of glass P2, and near multidomain for glass sample P4 and the other sub-sample of glass P2. Frequency dependence (fd%) peaks at 21% for P1, indicating abundant magnetite grains in the 20 nm size range (Hrouda and Pokorni, 2011) as found in oxidized impact glasses. fd% is minimal for glass sample P4. Wasp-waisted hysteresis cycle shape for glass samples P1 and P2 (Suppl. Fig. D) is typical of two components system in terms of grain size and coercivity, in agreement with the SEM

observations. Thermomagnetic curves (Suppl. Fig. E) reveal near reversible curves and sharp Curie points near 510 (glass sample P2) and 570 °C (glass sample P4) typical of weakly substituted and nearly pure magnetite, respectively. The regular decrease upon heating in the 20-400 °C range may correspond to a second category of grains with large variable substitution. Large grains of substituted (average x=0.5 based on SEM and microprobe) magnetite grains are responsible for the low Curie temperature trend (in the RT to 250°C range). Therefore, the micron-sized grains should correspond to the well-defined high Tc, i.e. small (x circa 0.05 for glass sample P2) and homogeneous substitution.

AF demagnetization of NRM of glass samples reveals univectorial decay toward the origin above about 20 mT and full demagnetization at 100 mT. Oriented subsamples from glass sample P2 show incoherent directions. NRM/ARM ratio at 28 mT are about 0.25 for glass samples P1 and P2, compared to 1.3 for glass sample P4. This signals a different mode of NRM acquisition (see discussion).

Polymict breccia and possible ejecta layer

The P5 breccia samples are polymict, with sub-angular millimeter- to decimeter-size clasts (Suppl. Fig. F). The majority of the clasts are volcanic rocks from the surrounding bedrock but some are Paleozoic metamorphic rocks, as observed in the putative ejecta, which includes schist and millimetre-size fragments of quartz. Many clasts possess an alteration rim and are enclosed in a whitish porous matrix that occupies more than 50% of the volume. Optical microscopy, BSE imaging and XRD results are consistent with an igneous or metamorphic origin for the clasts (feldspar, quartz, muscovite, garnet, hematite). Muscovite and garnet likely come from the Paleozoic schists as they have not been observed in the Matagalpa Group volcanic rocks.

In breccia sample P5, clasts displaying relict flow textures and vesicles are abundant (Figs. 9a–c). EDS analyses and XRD indicate these melts are completely replaced with quartz, analcime, cristobalite, potassium feldspar, goethite, and a clay, most likely montmorillonite (Fig. 9; Suppl. Fig. G). SEM investigation of a magnetic extract from breccia sample P5B reveal SiO_2-rich grains with fine Cr,Ni-bearing magnetite inclusions (suppl Fig. H).

Thin section observation of four cm-scale quartz fragments from the possible ejecta layer failed to identify planar deformation features (PDF) in quartz; nonetheless they appear strongly deformed with numerous planar fractures. Thin sections from six volcanic rock samples collected near the rim reveal no or very minor quartz and the search for PDF was unsuccessful.

Geochemistry

Water content determined by FTIR on glass samples P2 and P3 is 280 and 240 ± 20 ppm, respectively (Fig. 10). The calibration performed using the synthetic glass of Rapin et al. (2017) confirms that we were able to correctly estimate such very low water contents. Conversely, perlitic glass sample P4 yielded a water content > 1.6 %, after which the signal becomes saturated.

Major and trace elements were determined for four volcanic rock samples, P6, P9, P11 and P15 (from the TO site; see Fig. 1B and Table 2), three glass samples (P1, P2, P4), one polymict breccia sample (P5B) and one soil sample near the TO (P17). An average volcanic rock composition was computed from data for rock samples P4 to P15, and an average dry glass value from samples P1 and P2. An enrichment factor (EF) relative to the volcanic rock average was computed for the dry glass average, breccia, and soil samples. The EF values appear bold if significantly different from one (non overlapping

s.d.). In a NaO +K_2O versus SiO_2 diagram (Fig. 11) the rocks plot on the border between dacite to trachydacite and trachyandesite compositions. The P1 and P2 glass samples are displaced toward the dacite to andesite field due to a decrease of NaO content by a factor of 1.5 while K_2O is nearly identical. EDS analyses of P1 to P3 glasses reveal similar results (Fig. 11). The P4 glass appears also in the dacitic field, with a higher Na_2O and higher LOI than the P1-P3 glasses. It is not a typical obsidian but likely a chilled margin from a dacitic flow. Breccia sample P5B is enriched in SiO_2 and K_2O and depleted in all other major elements, relative to average volcanic rock. The soil is strongly depleted in SiO_2 and alkalis, and enriched in Al and Fe as well as other metallic elements (Ti, Mn, Cr, Co, Ni, Cu). The P1-P3 glasses appear to have a major element composition atypical for obsidians which are mostly in the rhyolite field, in particular the ones analyzed by Mrazova et al., (2011), and could be derived from rocks of P4-6-9-11-15 average composition. Indeed, the enrichment factor EF (Table 2) is not significantly different from 1, apart from Na_2O and LOI (below 1) as well as Cr and Ge (> 1). Incompatible trace element plots further establish the close parentage between glass samples P1-P2 and local volcanic rocks (suppl. Fig. I); a slight admixture of soil may explain the behavior of the more incompatible elements, as well as Cr and Ge excesses.

The $\varepsilon^{54}Cr$ value obtained for the terrestrial basalt standard BHVO-2, (0.07±0.13) is identical to previously reported values (0.07±0.07, Mougel et al. 2018) and is within uncertainty identical to the composition estimated for the bulk Earth (0.10±0.13; Mougel et al. 2018). On the other hand, polymict breccia sample P5B is relatively depleted in ^{54}Cr, with a $\varepsilon^{54}Cr$ value of -0.11±0.07 that is distinct from the terrestrial range (0.03 to 0.19, Mougel et al. 2018; Figure 12; suppl. Table D). Note that a wider range for terrestrial samples was reported in earlier publications (e.g. Trinquier et al., 2006; Foriel et al. 2013) due to larger uncertainties in the measurements. The negative

ε^{54}Cr measured in breccia sample P5B falls between terrestrial and ordinary chondrite compositions. It is therefore compatible with a fraction of Cr present in sample P5B being of ordinary chondrite parentage (note that a HED or ureilite parentage is also compatible but we follow the literature, e.g. Koeberl et al., 2007b, to consider these options very unlikely). The breccia shows indeed a strong EF for Cr, which may be due to the combined effect of extraterrestrial and metamorphic basement contamination. Significant EF >1 are also observed for Cu, Zn, Rb, Ba, Th, and EF<1 for Eu and U. This may indicate the effect of hydrothermal alteration.

^{40}Ar/^{39}Ar Geochronology

Two aliquots from glass sample P2 of ca. 10 and 20 mg yielded a plateau age of 821 ± 14 (P = 0.41) and a mini-plateau age of 806 ± 17 ka (P = 0.59), including 77% and 62% of the total ^{39}Ar released, respectively (Fig. 13). The second aliquot did not achieve a full plateau due to the presence of bubbles that contained inherited Ar and decrepited during analyses as shown by older isolated steps above 62% of total ^{39}Ar released (Fig. 11b). A third aliquot failed to yield a meaningful age and yielded older apparent step ages indicating the presence of significant amount of inherited ^{40}Ar*, probably coming from undigested clasts or bubbles (e.g., Jourdan et al., 2007). Although mini-plateau ages have been demonstrated to be less robust than plateau ages, the mini-plateau and plateau ages obtained in this study both agree within uncertainty thus supporting the validity of the mini-plateau age. We calculated a weighted mean age of 815 ± 11 ka (P = 0.17) as the best estimate of the formation age of the Pantasma glass.

DISCUSSION

Our investigation of the Pantasma structure revealed both diagnostic evidence of impact processes, as well as many other features that are suggestive of a recent impact event.

Two types of diagnostic evidence for impact were discovered in this study, based on the criteria listed in French and Koeberl (2010) or Reimold and Koeberl (2014). The first concerns high-pressure phases identified in the P1 and P2 glasses. Crystallographic evidence for the former presence of the high-pressure $ZrSiO_4$ phase reidite, that is preserved in the orientation relations of neoblasts in two granular zircon grains from glass sample P2. Detection of the former presence of reidite in granular zircon is a recently developed method that has been used to identify evidence of former reidite in glass from Meteor Crater (Cavosie et al., 2016), impact melt rock from the Acraman impact structure in Australia (Timms et al., 2017), and in Australasian tektites (Cavosie et al., 2018a). Such zircon grains are now referred to as FRIGN (former reidite in granular neoblastic) zircon, to distinguish their high-pressure and high-temperature origins (Cavosie et al., 2018b). Coesite identified by Raman spectroscopy in P1 further testifies for the high pressure recorded in these glasses.

The second diagnostic evidence for impact is the presence of an extraterrestrial Cr isotopic signal in the polymict breccia sample P5B, suggesting an ordinary chondrite impactor. Since the Cr isotopic composition of each meteorite group is distinct from the Earth (with the exception of enstatite chondrites, Mougel et al. 2018), and because Cr is much more abundant in chondrites than in the terrestrial crust, the presence of non-mass dependent Cr isotopic variations in terrestrial rocks is a very robust indicator of extra-terrestrial material (e.g. Shukolyukov and Lugmair 1998; Koeberl et al. 2007b; Trinquier et al. 2006; Moynier et al. 2009; Kyte et al. 2011; Foriel et al. 2013; Mougel et al. 2017; Magna et al. 2017). The intermediary $\varepsilon^{54}Cr$ of breccia sample P5B ($\varepsilon^{54}Cr$ = -

0.11± 0.07) between terrestrial rocks (0.02 <ε^{54}Cr< 0.19) and ordinary chondrites (ε^{54}Cr = -0.39 ± 0.12; Göpel et al. 2015) is therefore compatible with the presence of ordinary chondrite Cr in the breccia.

Production of the P1-P3 glasses by impact melting is further demonstrated by the following high-temperature criteria: 1) water content in the 240-280 ppm range. This excludes the glass from having a volcanic origin, as volcanic glass has been shown to have > 800 ppm H_2O (e.g. Shields et al., 2016). The low values measured here are typical of dry impact glasses (Beran and Koeberl, 1997); 2) presence of ZrO_2 inclusions within zircon from glass sample P2 as well as abundant lechatelierite within glass samples P1-P3, both of which require very high temperature, in excess of 1676 °C for zircon dissociation (Wittmann et al. 2006; Timms et al., 2017) and > 2000 °C for lechatelierite formation (Macris et al., 2018).

In contrast to the P1-P3 glasses, perlitic glass sample P4 is likely of volcanic origin, based on its petrography, water content (> 1400 ppm), different magnetic properties, higher Na_2O concentration and LOI. Further discrimination of volcanic and fulgurite origin for the dry glasses (P1-P3) is found in the different magnetic properties between glass samples P1-3 and P4. In particular while the high NRM/ARM ratio of glass sample P4 is typical of thermo-remanence acquired in cooling volcanic rocks, the low ratio in glass samples P1-P2 as well as incoherent direction may be the result of the cooling of a spinning ejected body. No sign of high field exposure typical of lightning (Verrier and Rochette, 2002) was detected.

The observed “granular magnetite” is likely also indicative of high temperature melting, however its formation conditions remain unknown. To our knowledge, such features have not been reported in terrestrial magmatic rocks, but are similar to what is observed in G type cosmic spherules (i.e. with equivalent oxide and silicated fractions;

Fig. 7d; Genge et al., 2008). They have also been described in glasses at the El'gygytgyn (Pittarrelo and Koeberl, 2013) and Zhamanshin (Kosterov et al., 2019) impact craters.

Siderophile element content in the impact glasses, with Co ≈ 10 ppm and Ni<Co, seems to exclude a significant impactor component. The volcanic rocks contain even lower abundances of siderophile elements. Ni and Co contents are on average 4 ppm, but a small contamination by soil could also explain the glass composition: in the analyzed soil Ni and Co contents are 13 and 24 ppm, respectively. We did not perform mixing calculation as the existing database besides rocks (two glasses with contrasting trace element contents and a single soil) is not deemed representative enough to evaluate quantitatively if the glass composition can be accounted for by a rock/soil mixture.

Other features compatible with an impact origin of the Pantasma structure include the following:

- a typical structure and associated deformation found at impact craters (outward dip of the Oligocene volcanic flows, faulting and folding, brecciation, possible ejecta layer containing deeply excavated Paleozoic material)
- the occurrence of polymict breccia in the center of the structure with altered melt fragments that broadly resembles suevite. The breccia also includes Paleozoic clasts, and its mineral assemblage is consistent with hydrothermal activity (presence of analcime, cristobalite, montmorillonite), especially considering the large and clear analcime crystals observed (Osinski et al., 2013), and the observed trace element EF (see Results section).

Although some of these supporting features could be of volcanic origin, the regional geology records no Quaternary volcanism in the area. We emphasize that the impact glasses (P1-P3) and extraterrestrial-chromium-contaminated breccia (P5B) were both found near the depression center, but were sampled from river gravels or boulders,

rather than in situ from outcrop. Thus their precise origins are unknown. However, the impact glass must be either locally derived or originate from upstream, within at most 15 km from the center of the structure based on the river catchment. This kind of glass ejection distance is typical for structures the size of Pantasma (Dressler and Reimold, 2001). The possibility that the glass originated from another impact structure is highly unlikely. The glass is deemed proximal based on its petrography, i.e. it cannot derive from long distance transport such as observed in tektites. For example the presence of Fe^{3+} and abundant scoriaceous inclusions is not typical of tektites, including Muong Nong type (e.g. Rochette et al., 2015, see also Table 3). The brecciated, partly recrystallized structures and presence of unmelted grains, including relict quartz, in P1 (Fig.4 and 5, suppl. Fig.B) further supports this claim. Rather than Muong Nong tektite, the best analog for the Pantasma impact glass may be the glasses described within the El'gygytgyn crater by Gurov and Koeberl (2004). These glasses may form large masses (up to 1 kg), with low vesicularity (relative density up to 2.5, comparable with values we measured on P1 and P2). They also show partial recrystallization and abundant unmelted inclusions, with significant ferromagnetic signal (our ongoing unpublished study, Table 1). Based on the proximal nature of Pantasma glass, the probability that a recent impact crater, which was able to launch impact glasses directly into the young Pantasma structure, while remaining unnoticed within a few tens of km from Pantasma seems negligible.

The $^{40}Ar/^{39}Ar$ data based on two successful aliquots yielded an age of 815 ± 11 ka for the impact glass. This is marginally, yet statistically indistinguishable, from the mean age of 777 ± 32 ka (2σ) obtained on a Belize tektite by Schwartz et al. (2016) thus a priori allowing a common origin. However, the analytical precision obtained on the

Belize tektites is less than ideal, preventing proper comparison with the Pantasma glass. Future studies (in progress) will attempt to refine the age of the Belize tektites for a better comparison with the Pantasma glass. At this stage we can only emphasize that based on petrography and magnetic properties (Table 1), the Pantasma glasses cannot be a distal ejecta, part of the Belize strewn field or any other know tektite strewn field (Rochette et al. 2015).

The Pantasma depression has been previously regarded as an Oligo-Miocene caldera based on its location within a belt of Oligocene volcanic and volcanoclastic rocks (Fig. 1a, Mapa Geológico Minero de la Republica de Nicaragua, INETER, 1995). We show in the following section that the morphology of the Pantasma structure is compatible with formation by impact cratering, and further show that its advanced stage of dissection remains compatible with the young age of the impact glass. We first determined whether the overall shape of the Pantasma structure is more akin to that of an impact crater or that of a volcanic crater by comparing some metrics of its morphology to that of a tropical impact structure of similar size and age, and to that of a nearby 5 Ma-old volcanic structure. We then applied numerical modeling to evaluate whether the stage of dissection of the crater is compatible with regional erosion rates.

We compare the Pantasma structure to the following structures (Fig. 14):

1) the 10.5 km diameter Bosumtwi impact crater in Ghana dated at 1.07 Ma (Koeberl et al., 2007a). According to these authors, Bosumtwi is the “best preserved complex young impact crater known on Earth” and its location in a tropical (6° North latitude) humid climate similar to Nicaragua highlands (13° North latitude) justifies its use as reference for our case.

2) a known late Tertiary 6 km diameter caldera from Nicaragua: Las Lajas, centered at 12°18’N and 85°44’W. Ehrenborg (1996) estimate that the caldera post-

dates 4.9 Ma and marks the end of the Coyol Group. Indeed, when finding circular depressions in volcanic regions one is naturally inclined to interpret such structures as a calderas.

To quantify the crater-like morphology independently of topographic irregularities, we devised a method whereby we averaged the altitude over a circle of increasing radius R, centered on the structure. We then plotted a relative altitude (zeroed at the lowest point of the profile, subtracted from water depth in the case of Lake Bosumtwi) as a function of normalized radius R/R_o, R_o being the radius of the crater structure (Fig. 15a). For Bosumtwi we used the published R_o of 5.25 km, while the other R_o were fitted to obtain the maximum slope at the same position (0.9 R_o as in Bosumtwi: Fig. 15b). Corresponding R_o values for Las Lajas and Pantasma are 3.00 and 7.25 km, respectively. For the calculation of the average altitude we used a 0.01 step on R/R_o with a subsequent smoothing on 5 steps.

Compared to Bosumtwi, the Pantasma profile shape is quite similar with a distant plateau reached at circa 2.5 R_o at a relative altitude of nearly 370 m (Fig. 15a). The lower corresponding value for Bosumtwi (210 m) can be linked to the fact that we did not subtract the lake sediment thickness of more than 200 m (Koeberl et al. 2007a). For these two cases the crater rim is marked by a moderate extra elevation with respect to the plateau, typical of crater wall uplift. Two humps are seen, with the higher and sharper near the crater, while the more distant one could be named a “rampart”. On the other hand the Las Lajas caldera exhibits a typical stratovolcano structure with a constant slope up to 3 R_o, i.e., with no plateau, and a central depression higher in altitude than the 3 R_o altitude. The quantitative geomorphological method illustrated here is therefore more consistent with the Pantasma depression being a mildly eroded impact crater, about 14 km in diameter (Figs. 1b and 14a).

Yet, based on comparison with the Bosumtwi structure, one may wonder why the Pantasma crater walls seem much more dissected, with no lake occupying the crater floor, which instead is filled by alluvial fans, and traversed by the Pantasma River. The two structures share similar ages (1.07 Ma vs. 0.815 Ma), receive similar amount of average annual rainfall, and experience similar climate seasonality (Bosumtwi: 1,260 mm/y, Shanahan et al., 2007, Pantasma: ~1,200 mm/y^{-1}, USGS-EROS climate hazards group InfraRed map). However, the Bosumtwi meteorite impacted a more subdued terrain (Fig. 14b), such that its rampart topographically isolates the interior from the surrounding river network. As a result, only inner crater walls contribute water to the lake that fills the crater. Due to this limited catchment, the lake is closed (inward draining) meaning that the balance between inflow and evaporation maintains its surface more than 100 m below the crater rim (Fig. 14b). Like all closed lakes, its surface amply fluctuates due to climate oscillations. It is possible that the lake was once able to overflow its northwest rim, through a 50m-deep breach (Fig. 14b), yet it never maintained a water balance positive enough to allow for protracted overflow, crater rim incision, and subsequent draining of the lake. Besides, as a result of this small catchment, little fluvial sediment contributes to filling of the lake, whose sedimentation is dominated by atmospheric and biogenic fallout (Otu, 2010). Conversely, the Pantasma crater was excavated in more mountainous terrain, where river courses are more deeply confined by surrounding topography. As a result, some of the rivers flowing towards the crater were not diverted around its rim but instead maintained their course to the structure, substantially contributing to its water and sediment budget. At its outlet the Pantasma depression drains a catchment (194 km^2) twice as large as the crater floor itself (100 km^2, Fig. 14a). The proposed impact crater likely initially hosted a lake, to which the fluvio-lacustrine sequence found near Las Praderas may belong. The larger

catchment of the Pantasma structure shortened the lifetime of this lake. The larger contributing catchment provided a more positive water balance, allowing for the lake to spill over the crater rim, and cut a 250m-deep outlet valley through which the lake drained away (Fig. 14a). This outlet reduced progressively to zero the volume of the initial lake. The velocity at which such incision proceeded is unknown but was probably fast, by analogy to currently observed caldera lake overflows (Manville et al., 2010). Rivers draining to the Pantasma structure also contributed more sediment to the lake than in the Bosumtwi case due to their more extensive and steep headwaters (mean slope of 17 ± 9°). They filled the lake, and built extensive alluvial fans that today straddle the entire crater floor.

To evaluate whether the significant amount of incision and infilling observed in the Pantasma structure is compatible with the proposed young age of ca. 800 ka, we conducted a numerical simulation of its erosion using *Badlands* (Salles and Hardiman, 2016; Salles et al., 2018), an open-source Python-based numerical framework (see Supplementary Material: numerical modeling of crater erosion). The numerical modeling results indicate that the amount of erosion of the Pantasma structure lies within the range expected for a steep, high erodibility, and wet tropical area. Further exploration of the crater floor through drilling, or gravity survey, can help refine these estimates, and reveal evidence for the eventual presence of a buried central peak made of Paleozoic schist and polymict breccia.

Starting from a scaling of the crater occurrence probability (based on lunar crater counts) and the distribution of Earth surface ages, Johnson and Bowling (2014) predict that all craters larger than 85 km diameter have already been discovered, while only one third of existing craters over 10 km diameter are known. In contrast, by taking into account erosion, Hergarten and Kenkmann (2015) proposed a threshold of 6 km

diameter, above which they predict that searching for new exposed craters will not change significantly the present count. Unexposed impact structures are not included in this prediction as they are protected from erosion by subsequent sedimentation. To reach this conclusion an average erosion rate of 60 m/Ma is needed. Does the discovery of the Pantasma crater following three other exposed craters > 10 km in diameter published since 2011 (Luizi, Santa Marta, Tunnunik; Earth Impact Database, 2018), invalidate this prediction?

Over a total continental surface of 133 Mkm^2 (not counting ice-covered Antarctica and Greenland), the present database of craters larger than 10 km diameter includes 68 entries (Earth Impact Database, 2018). This scales to 10 craters for a 20 Mkm^2 surface that corresponds to USA plus Canada, or Mexico plus South and Central America. The real numbers for these two equal surface areas are 22 and 4, respectively. Europe and Australia yield an even higher large crater density than USA plus Canada, while Asia and Africa mirror the low density of Mexico plus South and Central America (Table 3). Excluding unexposed craters in the statistics (as done by Hergarten and Kenkmann; 2015) does not significantly change the gap between the two continental groups highlighted in Table 3 with a factor ~5 between the densities of large exposed structures. Not taking into account the variability of average crustal ages, which should not reach a factor 5, it seems obvious that the vast majority of large exposed structures from Africa, Asia and America south of USA remain to be discovered. A simple scaling exercise produces ~70 large exposed craters yet to be discovered in these areas to reach the crater density of the other crater-rich continental areas. We therefore conclude that the fixed erosion rate of 60 m/Myr chosen by Hergarten and Kenkmann (2014) may not be accurate. Indeed, based on ^{10}Be in sediments, Willenbring et al. (2013) estimate a

global average of denudation rate of 19 m/Myr, while it tends to ~12 m/Myr for areas with slopes lower than 100 m/km, which covers 92% of the continental surface.

CONCLUSIONS

We propose that the Pantasma structure has an impact origin, based on 1) the identification of impact glasses by high pressure phases (former reidite in zircon; coesite) and high temperature criteria (water content below 300 ppm, presence of lechatelierite, high-temperature dissociated zircon) and 2) the presence of extraterrestrial Cr within a polymict former melt bearing breccia. Its age is 815 ± 11 ka and its diameter is circa 14 km with an original crater morphology still partly preserved. Originally horizontal Oligocene volcanic flows from the target surface have been deformed (with a systematic dip toward the exterior), brecciated, hydrothermally altered and melted by the impact. Impact excavation of underlying Paleozoic metamorphic rocks is evidenced by clasts found in the polymict breccias as well as within a possible ejecta layer.

Pantasma is only the third large (> 10 km) confirmed impact structure in the Pleistocene (and in the Quaternary), the two other being Bosumtwi and Zhamanshin (Earth Impact Database, 2018). Pantasma is the first impact structure from Central America, and the only known large impact structure exposed in tropical America between the latitude of N30° (Sierra Madera) and S8° (Serra de Cangalha). Regarding the significant deficit in crater density from continental areas outside Australia, Europe, and North America, our statistical analysis suggests that tens of exposed craters larger than 10 km remain to be discovered.

Acknowledgments: for their help with the field work we are deeply indebted to the Centre d'Etudes Mexicaines et Centro-Americaines (CEMCA) and its director S. Hardy, as

well as to C. Thomas. Field and laboratory studies were partly funded by ANR-15-CE31-0011-01 SVPINT MEX project and by A*Midex foundation from Aix-Marseille University. J. Gattacceca is thanked for the CAMPARIS microprobe measurements and N. Bezaeva for the magnetic measurements on El'Gygytgyn glass. AJC acknowledges support from the NASA Astrobiology program (grant NNAI3AA94A), the Space Science and Technology Centre, and the Microscopy and Microanalysis Facility in the John de Laeter Centre at Curtin University. VD thanks the FRS-FNRS and ERC StG "ISoSyC" FP7/336718 for present support. We thank Martin Bizzarro and Daniel Wiedlandt who generously analyzed the Cr isotopic ratios. Parts of FM and BM work were supported by IPGP platform PARI, and by Region Île-de-France Sesame Grant no. 12015908. BR acknowledges support from INSU through the national Raman facility in Lyon, and from the LABEX Lyon Institute of Origins (ANR-10-LABX-0066), within the program "Investissements d'Avenir" (ANR-11-IDEX-0007) at Université de Lyon. Geomorphological analyses were conducted in CEREGE with the support of P. Dussouilliez and J. Fleury from SIGeo service Geomorphological modeling was supported by the Australian Research Council grant #ARC-IH130200012 awarded to the Basin Genesis Hub, with resources from the National Computational Infrastructure (NCI) supported by the Australian Government and from Artemis HPC supported by the University of Sydney. We acknowledge in depth and constructive comments from reviewers A. Wittmann and B. Simonson, as well as associate editor M. Poelchau.

REFERENCES

Aggen K. L. 2007. Provenance sourcing of obsidian artifacts from Managua, Nicaragua, using trace element geochemistry. MSc thesis Colorado School of Mines, 224 pp. Available at https://dspace.library.colostate.edu/handle/11124/170372.

Arengi J. T. and Hodgson G. V. 2000. Overview of the geology and mineral industry of Nicaragua. *International Geology Review* 42:45-63.

Beran A. and Koeberl C. 1997. Water in tektites and impact glasses by Fourier-transform infrared spectroscopy. *Meteoritics & Planetary Science* 32:211–216.

Cavosie A. J., Timms N. E., Erickson T., Hagerty J. J. and Hörz F. 2016. Transformations to granular zircon revealed: Twinning, reidite, and ZrO_2 in shocked zircon from Meteor Crater (Arizona, USA). *Geology* 44: 703-706.

Cavosie A. J., Timms N. E., Erickson T. M., and Koeberl C. 2018a. New clues from Earth's most elusive impact crater: Evidence of reidite in Australasian tektites from Thailand. *Geology* 46: 203-206.

Cavosie A. J., Timms N. E., Ferrière, L., and Rochette, P. 2018b. FRIGN zircon, the only terrestrial mineral diagnostic of high-pressure and high-temperature of shock deformation. *Geology* 46: 891-894. https://doi-org.insu.bib.cnrs.fr/10.1130/G45079.1

Crosta A. P. and Vasconcelos M. A. R. 2013. Update on the current knowledge of the Brazilian impact craters. LPSC Abstract #1318.

Dressler B. D. and Reimold W. U. 2001. Terrestrial Impact Rocks and Glasses. *Earth Science Review* 56:205–284

Earth Impact Database, 2018. http://www.passc.net/EarthImpactDatabase/

Ehrenborg J. 1996. A new stratigraphy for the tertiary volcanic rocks of the Nicaraguan Highland. *Geological Society of America Bulletin* 108:830-842.

Elming S. A., Layer P. and Ubieta K. 2001. A palaeomagnetic study and age

determinations of Tertiary rocks in Nicaragua, Central America. *Geophysical Journal International* 147:294-309.

Erickson T. M., Pearce M. A., Reddy S. M., Timms N. E., Cavosie A. J., Bourdet J., Rickard W. D. A. and Nemchin, A. A. 2017. Microstructural constraints on the mechanisms of the transformation to reidite in naturally shocked zircon. *Contributions to Mineralogy and Petrology* 172 https://doi.org/10.1007/s00410-016-1322-0.

Folco L., Di Martino M., El Barkooky A., D'Orazio M., Lethy A., Urbini S., Nicolosi I., Hafez M., Cordier C., van Ginneken M., Zeoli A., Radwan A. M., El Khrepy S., El Gabry M., Gomaa M., Barakat A. A., Serra R. and El Sharkawi M. 2011. Kamil crater (Egypt): ground truth for small-scale meteorite impacts on Earth. *Geology* 39:179–182.

Foriel J., Moynier F., Schulz T., and Koeberl, C., 2013. Chromium isotope anomaly in an El'gygytgyn crater impactite: Evidence for a ureilite projectile. *Meteoritics & Planetary Science* 48: 1339-1350

French B. M., and Koeberl C. 2010. The convincing identification of terrestrial meteorite impact structures: What works, what doesn't, and why. *Earth Science Reviews* 98:123–170.

Genge M. J., Engrand C., Gounelle M. and Taylor S. 2008. The classification of micrometeorites. *Meteoritics & Planetary Science* 43:497–515.

Göpel C., Birck J. -L., Galy A., Barrat J. -A. and Zanda B. 2015. Mn-Cr systematics in primitive meteorites: insights from mineral separation and partial dissolution. *Geochimica et Cosmochimica Acta* 156: 1-24.

Gurov E. P. and Koeberl C. 2004. Shocked rocks and impact glasses from the El'gygytgyn impact structure, Russia. *Meteoritics & Planetary Science* 39:1495-1508.

Hergarten S. and Kenkmann T. 2015. The number of impact craters on Earth: Any room for further discoveries? *Earth and Planetary Science Letters* 425:187–192.

Hrouda F. and Pokorný J. 2011. Extremely high demands for measurement accuracy in precise determination of frequency-dependent magnetic susceptibility of rocks and soils. *Studia Geophysica Geod*etica 55:667–681.

Johnson B. C. and Bowling T. J. 2014. Where have all the craters gone? Earth's bombardment history and the expected terrestrial cratering record. *Geology* 42:587-590.

Jourdan F. and Renne P. R. 2007. Age calibration of the Fish Canyon sanidine $^{40}Ar/^{39}Ar$ dating standard using primary K-Ar standards. *Geochimica et Cosmochimica Acta* 71:387-402.

Jourdan F., Renne P. R. and Reimold U. W. 2007. The problem of inherited $^{40}Ar^*$ in dating impact glass by $^{40}Ar/^{39}Ar$ geochronology: Evidence from the Tswaing crater, South Africa). *Geochimica et Cosmochimica Acta* 71:1214-1231.

Koeberl C., Milkereit B., Overpeck J. T., Scholz C. A., Amoako P. Y. O., Boamah D., Danuor S. K., Karp T., Kueck J., Hecky R. E., King J., Peck J. A. 2007a. An international and multidisciplinary drilling project into a young complex impact structure: the 2004 ICDP Bosumtwi impact crater, Ghana, drilling project – an overview. *Meteoritics & Planetary Science* 42:483–511.

Koeberl, C., Shukolyukov, A., and Lugmair, G. W. 2007b. Chromium isotopic studies of terrestrial impact craters: Identification of meteoritic components at Bosumtwi, Clearwater East, Lappajärvi, and Rochechouart. *Earth and Planetary Science Letters* 256:534–546

Kosterov A., Starunov V. A., Sergienko E. S., Yanson S. Y., Markov G. P., Kharitonskii P. V., Sakhatskii A. S., Lezova I. E. and Shevchenko E. V. 2019. Magnetic properties of tektite-like impact glasses from Zhamanshin astrobleme, Kazakhstan. In D. Nurgaliev et al. (eds.), Recent Advances in Rock Magnetism, Environmental Magnetism

and Paleomagnetism, Springer Geophysics, https://doi.org/10.1007/978-3-319-90437-5_30.

Kowald L. 2006. A young meteorite impact crater in the old volcanic landscape of Nicaragua? Communication at www.pantasma.com.

Kyte F. T., Shukolyukov A., Hildebrand A. R., Lugmair G. W., and Hanova J., 2011. Chromium-isotopes in Late Eocene impact spherules indicate a likely asteroid belt provenance. *Earth and Planetary Science Letters* 302:279–286.

Macris, C. A., Asimow, P. D., Badro, J., Eiler, J. M., Zhang, Y., and Stolper, E. M., 2018. Seconds after impact: Insights into the thermal history of impact ejecta from diffusion between lechatelierite and host glass in tektites and experiments. *Geochimica et Cosmochimica Acta* 241:69-94.

Magna T., Zak K., Pack A., Moynier F., Mougel B., Peters S., Skala R., Jonasova S., Mizera J., Randa Z. 2017. Zhamanshin astrobleme provides evidence for carbonaceous chondrite and post-impact exchange between ejecta and Earth's atmosphere. *Nature Communications* DOI: 10.1038/s41467-017-00192-5.

Manville V. 2010. An overview of break-out floods from intracaldera lakes. *Global and Planetary Change* 70:14-23.

McMillan, P.F., Wolf, G.H., Lambert, P., 1992. A Raman spectroscopic study of shocked single crystalline quartz. *Physics and Chemistry of Minerals* 19:71-79.

Mougel B., Moynier F., Göpel C. and Koeberl C. 2017. Chromium isotope evidence in ejecta deposits for the nature of Paleoproterozoic impactors. *Earth and Planetary Science Letters* 460:105-111.

Mougel B., Moynier F., Göpel C. 2018. Chromium isotopic homogeneity between the Moon, the Earth, and the enstatite chondrites. *Earth and Planetary Science Letters* 481:1-8.

Moynier F., Koeberl C., Quitté G., and Telouk P. 2009. A tungsten isotope approach to search for meteoritic components in terrestrial impact rocks. *Earth and Planetary Science Letters* 286:35-40.

Mrazova S. and Gadas P. 2011. Obsidian balls (marekanite) from Cerro Tijerina, central Nicaragua: petrographic investigations. *Journal of Geosciences* 56:43-49.

Osinski G. R., Tornabene L. L., Banerjee N. R., Cockell C. S., Flemming R. L., Izawa M. R. M., McCutcheon J., Parnell J., Preston L. J., Pickersgill A. E., Pontefract A., Sapers H. M. and Southam G. 2013. Impact-generated hydrothermal systems on Earth and Mars. *Icarus* 224:347-363.

Osinski G. R. and Ferrière L. 2016. Shatter cones: (Mis)understood? *Science Advances* 2, e1600616.

Otu M. K. 2010. The origin, transformation and deposition of sediments in Lake Bosomtwe/Bosumtwi (Ghana, West Africa). PhD, University of Waterloo, Ontario, Canada, 185 pp.

Pilkington M. and Grieve R. A. F. 1992. The geophysical signature of terrestrial impact craters. *Reviews of Geophysics* 30:161–181.

Pittarello L. and Koeberl C. 2013. Petrography of impact glasses and melt breccias from the El'gygytgyn impact structure, Russia. *Meteoritics & Planetary Science* 48:1236-1250.

Povenmire H., Harris R. S. and Cornec J. H. 2011. The new Central American tektite strewn field. In: 42th Lunar and Planetary Science Conference. Abstract #1224.

Rapin W., Meslin P. Y., Maurice S., Wiens R. C., Laporte D., Chauviré B., Gasnault O., Schröder S., Beck P., Bender S., Beyssac O., Cousin A., Dehouck E., Drouet C., Forni O., Nachon M., Melikechi N., Rondeau B., Mangold N. and Thomas N. H. 2017. Quantification

of water content by laser induced breakdown spectroscopy on Mars. *Spectrochimica Acta Part B Atomic Spectroscopy* 130:82-100.

Reimold W. U. and Koeberl C. 2014. Impact structures in Africa: A review. *Journal of African Earth Sciences* 93:57–175.

Renne P. R., Mundil R., Balco G., Min K. and Ludwig K. R. 2010. Joint determination of 40K decay constants and 40Ar*/40K for the Fish Canyon sanidine standard, and improved accuracy for 40Ar/39Ar geochronology. *Geochimica et Cosmochimica Acta* 74: 5349–5367.

Renne P. R., Balco G., Ludwig K. R., Mundil R. and Min K. 2011. Response to the comment by W.H. Schwarz et al. on "Joint determination of K-40 decay constants and Ar-40*/K-40 for the Fish Canyon sanidine standard, and improved accuracy for Ar-40/Ar-39 geochronology" by PR Renne et al. (2010). *Geochimica Cosmochimica Acta* 75:5097-5100.

Robbins S. J. and Hynek B. M. 2012. A new global database of Mars impact craters≥1 km: 1. Database creation, properties, and parameters. *Journal Geophysical Research* 117:E05004.

Robbins S. J. 2018. A global lunar crater database, complete for craters ≥1 km, iii: reassessing the lunar crater production function, and lessons learned applied to the global Mars crater database. LPSC conference, Houston, abstract #2443.

Rochette P., Folco L., Suavet C., van Ginneken M., Gattacceca J., Perchiazzi N., Braucher R. and Harvey R. 2008. Micrometeorites from the Transantarctic Mountains. *Proceedings of the National Academy of Sciences* 105:18206-18211.

Rochette P., Gattacceca J., Devouard B., Moustard F., Bezaeva N. S., Cournède C. and Scaillet B. 2015. Magnetic properties of tektites and other related impact glasses. *Earth and Planetary Science Letters* 432:381–390.

Saginor I. , Gazel E., Carr M. J., Swisher III C. C. and Turrin N. 2011. New Pliocene-Pleistocene 40Ar/39Ar ages fill in temporal gaps in the Nicaraguan volcanic record. *Journal of Volcanology and Geothermal Research* 202:143-152.

Salles T. and Hardiman L. 2016. Badlands: An open-source, flexible and parallel framework to study landscape dynamics. *Computers & Geosciences* 91:77-89.

Salles T., Xuesong D, Brocard G. 2018. PyBadlands: a framework to simulate sediment transport, landscape dynamics and basin stratigraphic evolution through space and time. *PloS one*, 13(4), p.e0195557.

Schwarz W. H., Trieloff M., Bollinger K., Gantert N., Fernandes V. A., Meyer H. P., Povenmire H., Jessberger E. K., Guglielmino M. and Koeberl C., 2015. Coeval ages of Australasian, Central American Canadian tektites reveal multiple impacts 790 ka ago. *Geochimica Cosmochimica Acta* 178:307-319.

Shanahan T. M., Overpeck J. T., Sholz C., Sharpe E. and Arko J. 2007. Simulating the response of a closed basin lake to recent climate changes in tropical West Africa (Lake Bosumtwi, Ghana). *Hydrologic Processes* 21:1678–1691.

Sharma S. K., Mammone J. F. and Nicol M. 1981. Raman investigation of ring configurations in vitreous silica. *Nature* 292:140-141.

Shields J. K., Mader H. M., Caricchi L., Tuffen H., Muller S., Pistone M. and Baumgartner L. 2016. Unravelling textural heterogeneity in obsidian: Shear-induced outgassing in the Rocche Rosse flow. *Journal of Volcanology and Geothermal Research* 310:137-158.

Shukolyukov A., and Lugmair G. W. 1998. Isotopic evidence for the Cretaceous-Tertiary impactor and its type. *Science* 282:927-930

Timms N. E., Erickson T. M., Pearce M. A., Cavosie A. J., Schmieder M., Tohver E., Reddy S. M., Zanetti M., Nemchin A. and Wittmann A. 2017. A pressure-temperature phase diagram for zircon at extreme conditions. *Earth-Science Reviews* 165: 185-202.

Trinquier A., Birck J. -L., and Allègre C. J. 2006. The nature of the KT impactor. A ^{54}Cr reappraisal. *Earth Planetary Science Letters* 241:780–788.

Trinquier A., Birck J. -L., and Allègre C. J., 2007. Widespread ^{54}Cr heterogeneity in the inner solar system. *The Astrophysical Journal* 655:1179.

Van Kooten, E., Wielandt, D., Schiller, M., Nagashima, K., Thomen A., Larsen, K., Olsen, M., Nordlund, A., Krot, A. and Bizzarro, M. 2016. Isotopic evidence for primordial molecular cloud material in metal-rich carbonaceous chondrites. *Proceedings of the National Academy of Sciences* 113:2011-2016.

Verrier V. and Rochette P. 2002. Estimating peak currents at Ground Lightning Impact using Remanent Magnetization. *Geophysical Research Letters* 29:10.1029/2002GL015207.

Werner T. and Borradaile G.J. 1998. Homogeneous magnetic susceptibilities of tektites: implications for extreme homogenization of source material. *Physics Earth Planetary Interior* 108:235–243.

Willenbring J. K., Codilean A. T. and McElroy B. 2013. Earth is (mostly) flat: Apportionment of the flux of continental sediment over millennial time scales. *Geology* 41:343-346.

Wittmann A., Kenkmann T., Schmitt R. T. and Stöffler D. 2006. Shock-metamorphosed zircon in terrestrial impact craters. *Meteoritics & Planetary Science* 41: 433-454.

Figure captions

Fig. 1. a) Geological map of North Central Nicaragua with the catchment of Pantasma depression (Mapa Geológico Minero de la Republica de Nicaragua, INETER, 1995), modified (Elming *et al.*, 2001; Ehrenborg, 1996). Inset: location of the Pantasma structure in Central America. b) Outcrop map of the Pantasma structure with bedding (dip angle in degree, whited) and lithologies indicated on the topography (brown is higher). Bold numbers highlighted in green correspond to rock samples in outcrops, or river bank floats (P1 to P5). Torre de oscilación (TO) and Quarry (Q) are indicated (highlighted in yellow). Position of the structure center is 13°22'N and 85°57'W.

Fig. 2. Trachytic flow outcrops at the TO excavation highlighting bedding (dashed lines): a) recumbent fold; b) vertical fault with 30 cm thick gouge of crushed rock. Pantasma river samples: c) glass samples (P1 to 3 by order of decreasing size); d) P5A polymict breccia boulder.

Fig. 3. a) and b) Transmitted light images of glass samples P3 and P1; c) to f) SEM backscatter images of P1 (c), P2 (d) and P3 (e-f) glass samples. Lechatelierite grains are identified by arrows. Note also the heterogeneous vesicular clast in the upper left side of c).

Fig.4: a and b) SEM backscatter images of P1 brecciated zones with examples of recrystallized glass (rg) and unmelted grains of amphibole (A), titanomagnetite (M) and quartz (Q).

Fig.5: a) Typical Raman spectra of silica clasts in breccia P1. b) coesite-rich clast. Scale bar 20 microns. c) lechatelierite clast. d) quartz clast with homogeneous grey center and polycrystalline rims. Note the bad polishing on clast rims and on lechatelierite likely due to the mechanical contrast with the glassy matrix.

Fig. 6. SEM backscattered electron images of a granular neoblastic zircon from Pantasma glass sample P2. a) Image of the whole grain, surrounded by glass. b) Close-up showing wide-spread occurrence of ZrO_2(bright inclusions), produced by partial dissociation of zircon at high-temperature. c) Close-up showing coarsening of neoblasts near an incursion of glass. d) Close-up showing area with ZrO_2 and vesicles.

Fig. 7. Orientation data for the granular neoblastic zircon shown in Figure 4. a) Orientation map showing variations in crystallographic orientation as a function of color. b) Close-up showing boundaries between neoblasts with misorientation relationships characteristic of reverted reidite (90°/<110>) and {112} twins (65°/<110>). c) Pole figures (lower hemisphere, equal area) showing data from (b). Note the three orthogonal orientations and coincidence of pole clusters for poles to both (001) and {110}. d) Misorientation plots showing that high-angle misorientations coincide with clusters of poles for {110}.

Fig. 8. SEM backscattered electron images of (a to c) iron oxides within glass sample P2 with a large (composite) grain in the center and sub-micron grains spread throughout the glass, and (d) iron oxides within G-type micrometeorites from Antarctica (d; unpublished sample from collection described in Rochette et al. 2008).

Fig. 9. SEM backscattered electron images of polymict breccia sample P5B. a) An angular shard-like clast displaying remnant flow and vesicle textures. White triangles point to the edge of the clast. The clast is completely altered to Na- and K-bearing zeolites and quartz. b) Close-up of the clast shown in a. c and d) Vesicular clast, altered to a combination of analcime (An), quartz (Qtz), clay (Cl), and goethite (Go). e and f) The groundmass of the breccia is completely altered to analcime, potassium feldspar (Kfl) and quartz.

Fig. 10. Transmission spectra of Pantasma glasses P2 and P3 (red spectra) showing the presence of an -OH absorption feature (see inset). The spectra of the glasses are compared to those of synthetic basaltic glasses with different H_2O abundance in black [Rapin et al., 2017]. The transmission spectrum of the P4 glass is also shown (blue spectra).

Fig. 11. Na_2O+K_2O versus SiO_2 plot for Pantasma dry glass samples P1-P3 (circles), rocks, P4 glass and soil (black, blue and brown diamonds) as well as Mrazova et al. (2011) obsidian (red squares; maximum and minimum values). For the glasses, ICPMS data are shown as a big circle, whereas SEM EDS data are shown as a small circle. Soil data is corrected for LOI.

Fig. 12. $\varepsilon^{54}Cr$ data for the breccia sample P5B. Data for terrestrial samples (basalts and peridotites, Mougel et al. 2018) are also shown as well as the composition of Ureilite, HED, ordinary and carbonaceous chondrites. P5B is isotopically distinct from the terrestrial samples.

Fig. 13. $^{40}Ar/^{39}Ar$ age spectra of three glass aliquots (10 mg, 20 mg and 40 mg) of sample P2. The combined weighted mean age of aliquots P2-10 mg and P2-20mg is 815 ± 11 ka (P=0.17). Errors are at the 2σ level and include all sources of uncertainties. Ages were calculated using the decay constants of Renne et al. (2011).

Fig. 14. Topographic maps of the Pantasma structure (a), Bosumtwi impact crater (b) and Las Lajas caldera (c). Contour line spacing: 100 m. Colour scale: elevation relative to the lowest point of each map. Numbers: elevation a.s.l. Red line: crater watershed. Blue line: outlet river (dashed: speculative past outlet). Dashed black lines: circles with diameters of 14.5, 10.5 and 6 km, centred (reticules) at W 85.948° N13.364°, W 85.727° N12.306°, and W 1.412° N 6.502 respectively.

Fig. 15. a) Relative average altitude over a given circle centered on the structure versus normalized radius (see text) for Bosumtwi, Las Lajas and Pantasma structures. b) Slope versus normalized radius.

Table 1. Bulk density and room temperature magnetic properties of the glass samples from this study as well as tektite-like glass of Belize (after Rochette et al., 2015) and Muong Nong tektite (after Werner and Borradaile, 1998). Belize and Muong Nong densities were measured by us.

sample	m (g)	ρ ($10^{\square}$ $kg/m^{\square}$)	χ (10^{-6} m^3/kg)	M_s (mAm^2/kg)	M_{rs}/M_s %	B_c (mT)	B_{cr} (mT)	χ_{hf} (10^{-9} m^3/kg)	fd%	NRM/ARM at 28 mT
P1	64	2.46	8.5-13.5	300	12	5	38	123	6.5	0.25
P2	29	2.55	20-25.6	830-926	6-12	3-5	37-45	236-257	21-23	0.24
P3	3.6	-	0.37	26	21	15	29	100	2.8	-
P4	205	-	6.9	702	6.5	7	44	135	2	1.31
Belize glass		2.34-2.55	0.11-0.14	<0.3				111	<2	
Muong Nong		2.45	0.08-0.10	<5				60-96	<2	
El Gygytgyn glass		2.40-2.50	0.18-4.46	42-80	3-5	3-7	31-36	57-84	6-12	

Table 2: geochemical data (major and trace elements) including average and s.d. for P1-P2 dry glasses and volcanic rock (P6 to P15 plus P4 glass. Enrichment factors EF are ratio to the average rock.

	P1	P2	dry glass mean	s.d.	EF dry glass	P4	P6	P9	P11	P15	rock mean	s.d.	P5B breccia	P17 soil	EF breccia	EF soil
SiO2	67.38	62.08	64.73	7.50	0.99	66.10	62.92	62.22	68.16	67.91	65.46	5.54	75.08	38.74	**1.15**	0.57
TiO2	0.57	0.81	0.69	0.34	0.91	0.63	1.05	0.95	0.36	0.83	0.76	0.55	0.13	1.64	**0.17**	**1.98**
Al2O3	14.82	15.47	15.15	0.92	1.05	14.07	13.90	15.59	14.61	13.89	14.41	1.44	11.57	20.30	0.80	**1.46**
FeO	4.81	6.89	5.85	2.95	1.19	3.02	6.61	7.92	2.70	4.41	4.93	4.55	2.57	14.16	0.52	**3.21**
MnO	0.10	0.11	0.10	0.03	0.93	0.12	0.10	0.16	0.08	0.10	0.11	0.06	0.04	0.18	0.32	**1.82**
MgO	1.34	2.35	1.85	1.43	2.09	0.67	0.82	1.38	0.62	0.92	0.88	0.61	0.52	1.80	0.59	1.96
CaO	3.63	4.91	4.27	1.81	1.85	2.06	0.65	4.00	2.26	2.53	2.30	2.40	0.47	0.78	**0.20**	0.31
Na2O	2.97	3.98	3.48	1.42	**0.69**	5.06	5.80	4.46	4.57	5.13	5.01	1.07	2.49	0.15	0.50	**0.03**
K2O	3.07	2.32	2.69	1.07	1.06	2.60	2.55	2.15	2.82	2.57	2.54	0.48	3.65	0.89	**1.44**	0.35
P2O5	0.10	0.17	0.13	0.09	0.75	0.09	0.28	0.24	0.08	0.20	0.18	0.18	0.03	0.10	**0.16**	0.48
LOI corr	0.64	1.12	0.88	0.68	**0.24**	6.21	4.51	2.49	2.27	3.04	3.70	3.30	4.01	22.48	1.08	**7.41**
total	99.44	100.21	99.82	1.09	1.00	100.63	99.19	101.56	98.54	101.52	100.29	2.74	100.55	101.22	1.00	1.00

ppm	P1	P2	dry glass mean	s.d.	EF dry glass	P4	P6	P9	P11	P15	rock mean	s.d.	P5B breccia	P17 soil	EF breccia	EF soil
Cr	9.5	20.5	15.0	15.5	**8.73**	0.5	3.5	1.9	2.1	1.4	1.7	1.0	40.4	12.6	**23.54**	**7.35**
Co	6.4	14.4	10.4	11.3	2.48	1.2	6.5	8.4	4.8	3.6	4.2	1.7	8.6	23.5	**2.04**	**5.60**
Ni	4.0	11.3	7.7	10.3	1.69	13.1	4.4	14.8	4.9	4.2	4.5	1.1	3.8	13.2	0.84	**2.90**
Cu	12.1	26.5	19.3	20.4	1.93	15.1	13.7	7.6	10.7	9.2	10.0	2.1	44.3	107.0	**4.44**	**10.72**
Zn	83.4	85.8	84.6	3.3	1.64	64.3	68.5	92.7	45.0	58.3	51.6	18.8	78.1	86.1	**1.51**	**1.67**
Ga	17.3	18.4	17.9	1.6	1.04	17.4	15.4	19.1	18.2	16.2	17.2	2.9	14.5	22.4	0.84	1.31
Ge	1.17	1.43	1.30	0.36	**1.52**	0.8	0.8	1.0	0.9	0.9	0.9	0.0	1.0	1.3	1.11	**1.55**
Rb	93.8	64.0	78.9	42.1	1.19	96.5	44.7	49.6	77.5	55.4	66.5	31.2	114.6	41.0	1.72	0.62
Sr	272	324	298	74	1.40	222	118	288	205	221	213	22	87.4	67.7	0.41	**0.32**
Y	31.4	28.2	29.8	4.4	1.15	41.8	34.3	30.4	22.7	29.4	26.0	9.5	25.6	22.1	0.98	0.85
Zr	196.3	174.7	185.5	30.6	1.20	233.9	174.1	148.5	127.8	182.2	155.0	77.0	179.2	182.3	1.16	1.18
Nb	7.00	6.14	6.57	1.22	1.50	6.39	6.51	5.32	3.71	5.02	4.37	1.85	6.35	5.85	1.45	1.34
Ba	828	700	764	182	1.09	884	664	611	796	601	699	276	3365	311	**4.82**	**0.44**
La	22.4	18.7	20.5	5.2	1.31	20.9	25.5	17.2	14.4	16.9	15.6	3.5	19.7	13.1	1.26	0.84
Ce	45.2	37.6	41.4	10.7	1.29	43.4	50.9	36.1	29.2	35.0	32.1	8.2	42.5	33.6	1.33	1.05
Pr	6.3	5.3	5.8	1.3	1.25	6.4	7.3	5.2	3.9	5.4	4.7	2.1	5.5	3.6	1.19	0.77
Nd	26.8	22.6	24.7	5.9	1.29	27.8	31.1	22.7	15.0	23.2	19.1	11.6	21.9	13.9	1.15	0.73
Sm	5.49	5.11	5.30	0.54	1.13	6.88	7.02	6.44	3.64	5.75	4.70	2.98	5.15	2.98	1.10	0.63
Eu	1.45	1.42	1.44	0.03	1.00	1.92	1.68	1.79	1.11	1.77	1.44	0.94	0.69	0.94	0.48	0.65
Gd	5.30	4.90	5.10	0.57	1.15	6.54	6.93	5.40	3.36	5.50	4.43	3.02	4.94	3.47	1.12	0.78

Tb	0.98	0.90	0.94	0.11	1.14	1.31	1.11	1.03	0.62	1.03	0.82	0.57	0.78	0.62	0.95	0.76
Dy	5.88	5.28	5.58	0.85	1.16	7.08	6.49	6.03	3.84	5.76	4.80	2.71	4.94	3.73	1.03	0.78
Ho	1.20	1.08	1.14	0.17	1.15	1.58	1.43	1.15	0.80	1.17	0.99	0.53	1.00	0.89	1.01	0.90
Er	3.49	3.21	3.35	0.40	1.12	4.61	3.95	3.56	2.57	3.42	2.99	1.21	2.92	2.42	0.97	0.81
Tm	0.54	0.54	0.54	0.00	1.20	0.71	0.52	0.46	0.40	0.51	0.45	0.16	0.49	0.34	1.09	0.76
Yb	3.57	3.46	3.52	0.16	1.11	4.98	3.86	3.47	2.95	3.40	3.17	0.64	2.96	2.27	0.93	0.72
Lu	0.62	0.53	0.58	0.13	1.19	0.71	0.51	0.54	0.42	0.56	0.49	0.20	0.44	0.32	0.91	0.65
Hf	4.92	4.32	4.62	0.85	1.19	6.02	4.49	3.93	3.26	4.52	3.89	1.78	5.52	4.48	1.42	1.15
Ta	0.63	0.54	0.59	0.12	1.60	0.56	0.61	0.42	0.35	0.38	0.37	0.05	0.65	0.45	1.77	1.24
Pb	10.6	7.9	9.2	3.8	1.36	8.7	9.8	8.1	6.9	6.7	6.8	0.3	10.4	7.6	1.52	1.12
Th	6.1	4.3	5.2	2.6	1.11	5.4	7.5	3.8	6.2	3.3	4.7	4.1	8.2	3.0	1.73	0.65
U	1.8	1.6	1.7	0.3	1.00	2.2	2.5	1.3	2.0	1.4	1.7	0.9	1.1	1.4	0.66	7.35

Table 3. Statistics on craters >10 km diameter for different Earth continental areas (excluding Antarctica and Greenland) based on www.passc .net /EarthImpactDatabase. Russia west of Ural was counted in Europe. "America (rest)" stands for all countries of the Americas except Canada and USA.

Continental area	Surface (Mkm^2)	N craters	not exposed	Density (crater/Mkm^2)	Density exposed
USA+Canada	20	22	11	1.1	.6
Europe	10	16	8	1.6	.8
Australia	9	11	2	1.2	1
sum	*39*	*49*	*21*	***1.3***	***.7***
Asia	44	8	3	.18	.11
Africa	30	7	1	.23	.2
America (rest)	20	4	1	.2	.15
sum	*94*	*19*	*5*	***.2***	***.15***
all	*133*	*68*	*26*	*.51*	*.32*

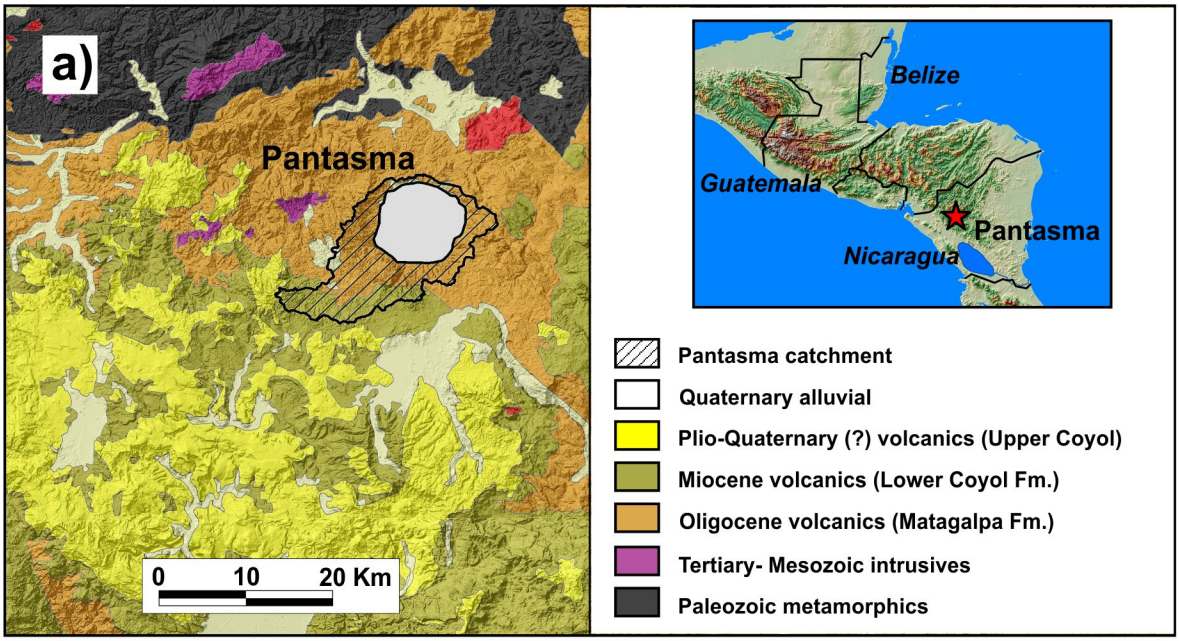
a)
Pantasma
0 10 20 Km
Belize
Guatemala
Pantasma
Nicaragua
Pantasma catchment
Quaternary alluvial
Plio-Quaternary (?) volcanics (Upper Coyol)
Miocene volcanics (Lower Coyol Fm.)
Oligocene volcanics (Matagalpa Fm.)
Tertiary- Mesozoic intrusives
Paleozoic metamorphics

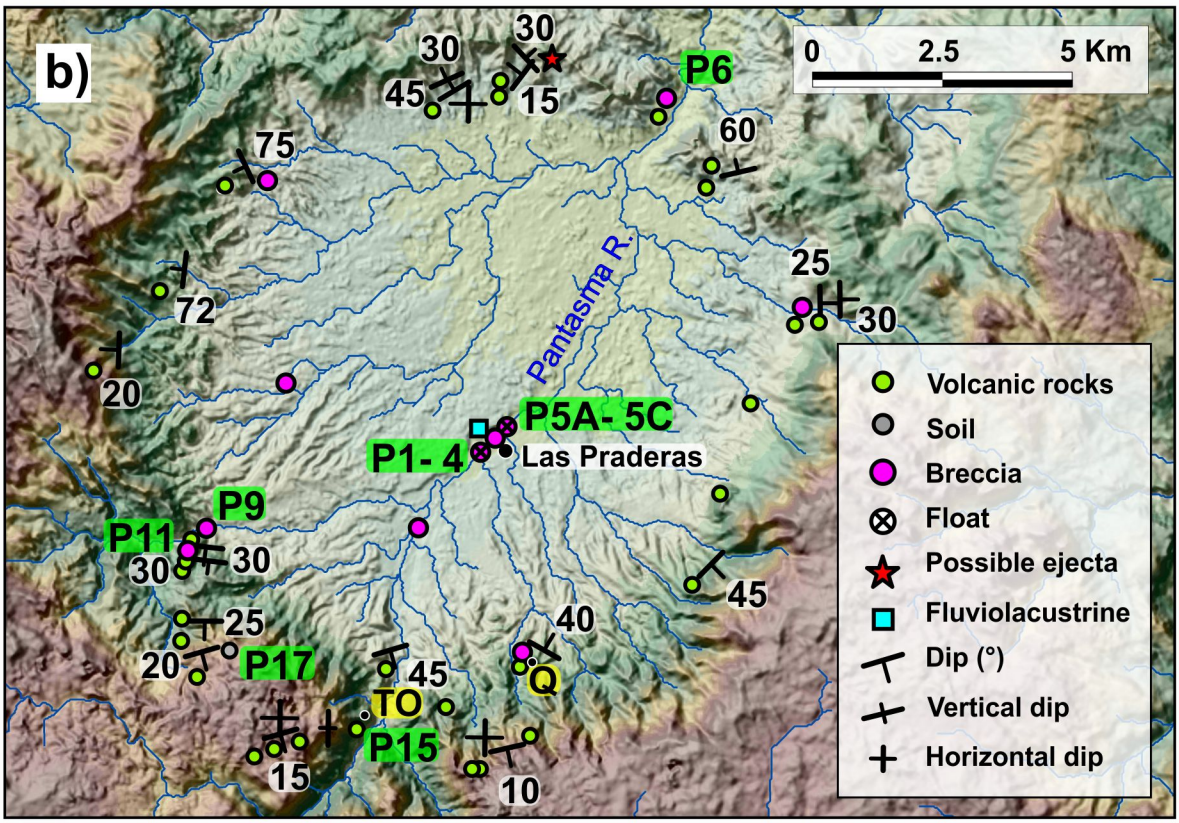
b)
0 2.5 5 Km
Pantasma R.
P6
P5A- 5C
P1- 4
Las Praderas
P9
P11
P17
TO
P15
Q
Volcanic rocks
Soil
Breccia
Float
Possible ejecta
Fluviolacustrine
Dip (°)
Vertical dip
Horizontal dip

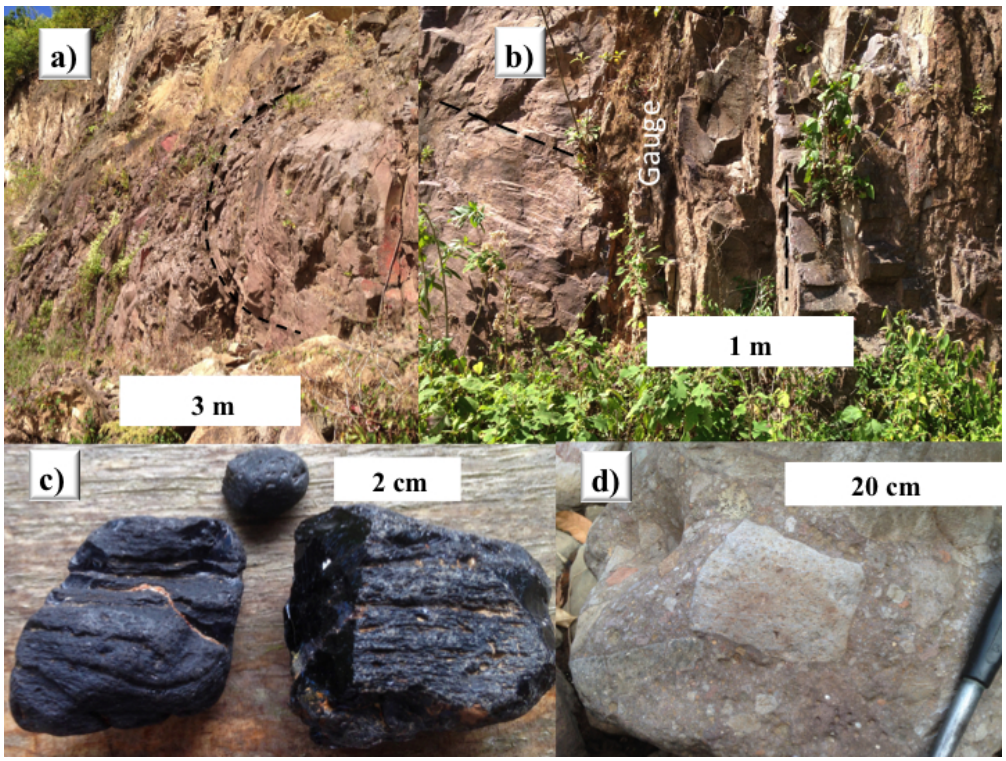

Fig. 2. Trachytic flow outcrops at the TO excavation highlighting bedding (dashed lines): a) recumbent fold; b) vertical fault with 30 cm thick gouge of crushed rock. Pantasma river samples: c) glass samples (P1 to 3 by order of decreasing size); d) P5A polymict breccia boulder.

254x190mm (72 x 72 DPI)

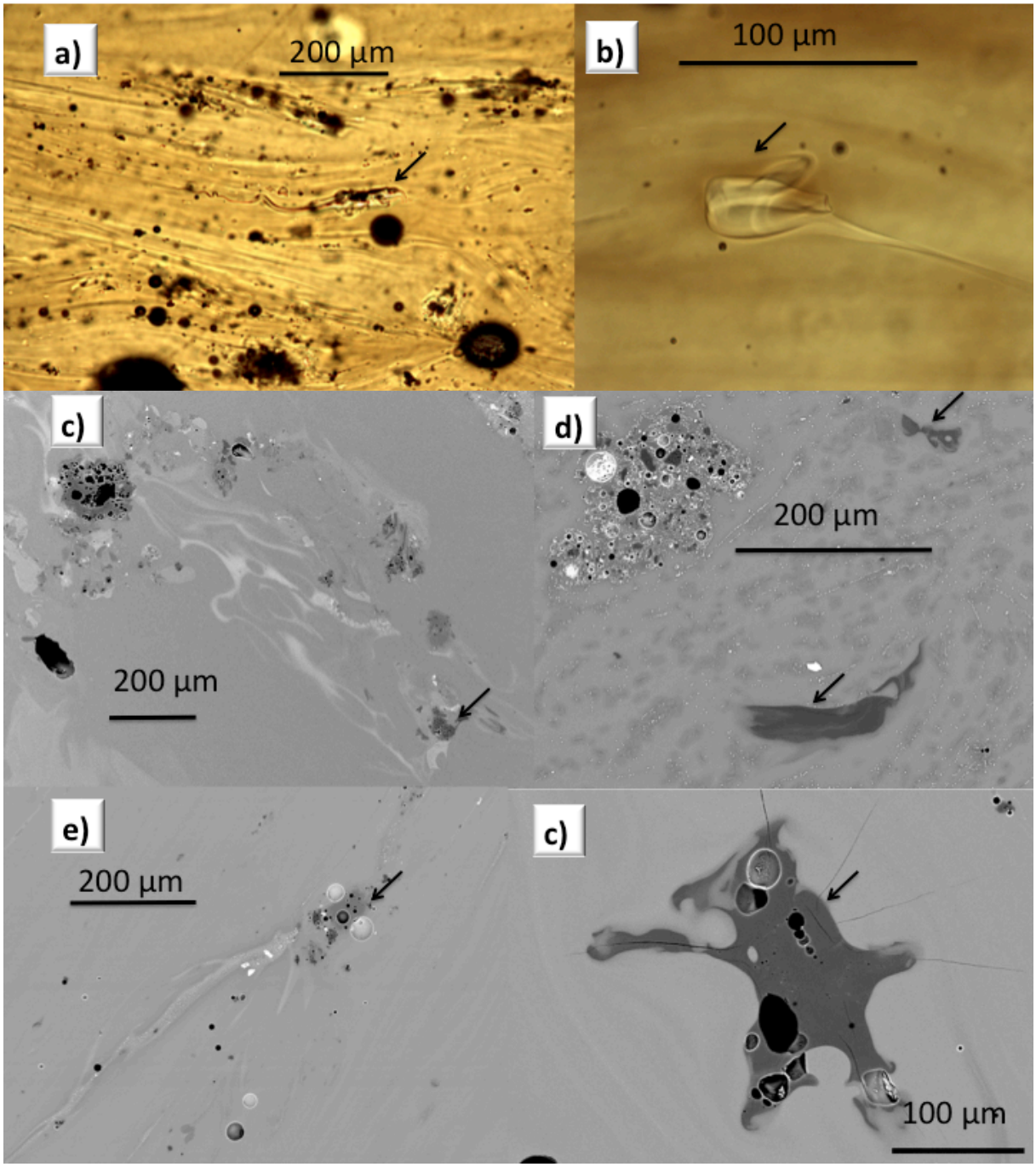
a)
200 µm
b)
100 µm
c)
200 µm
d)
200 µm
e)
200 µm
c)
100 µm

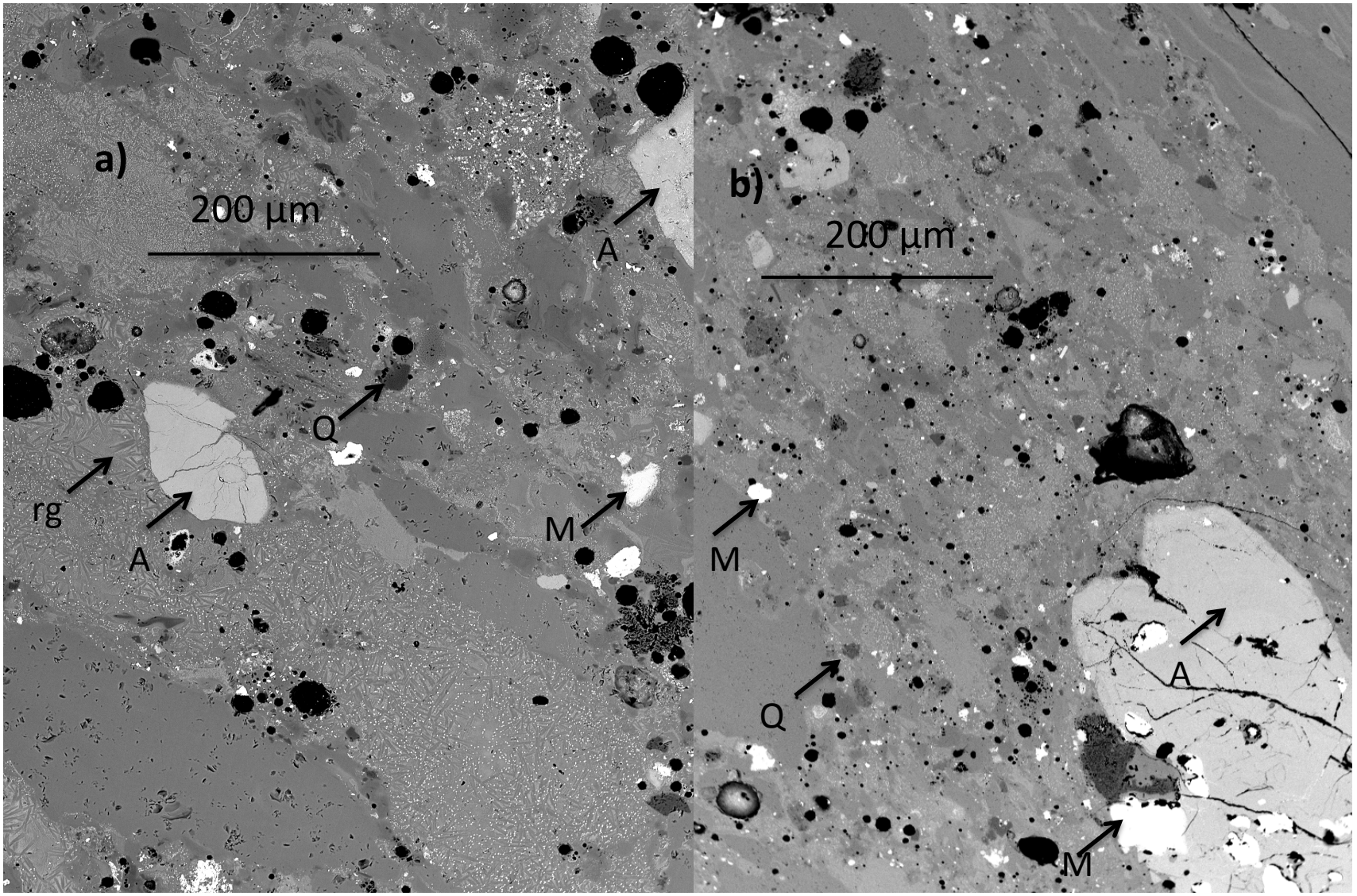
a)
200 µm
A
Q
rg
A
M
b)
200 µm
M
A
Q
M

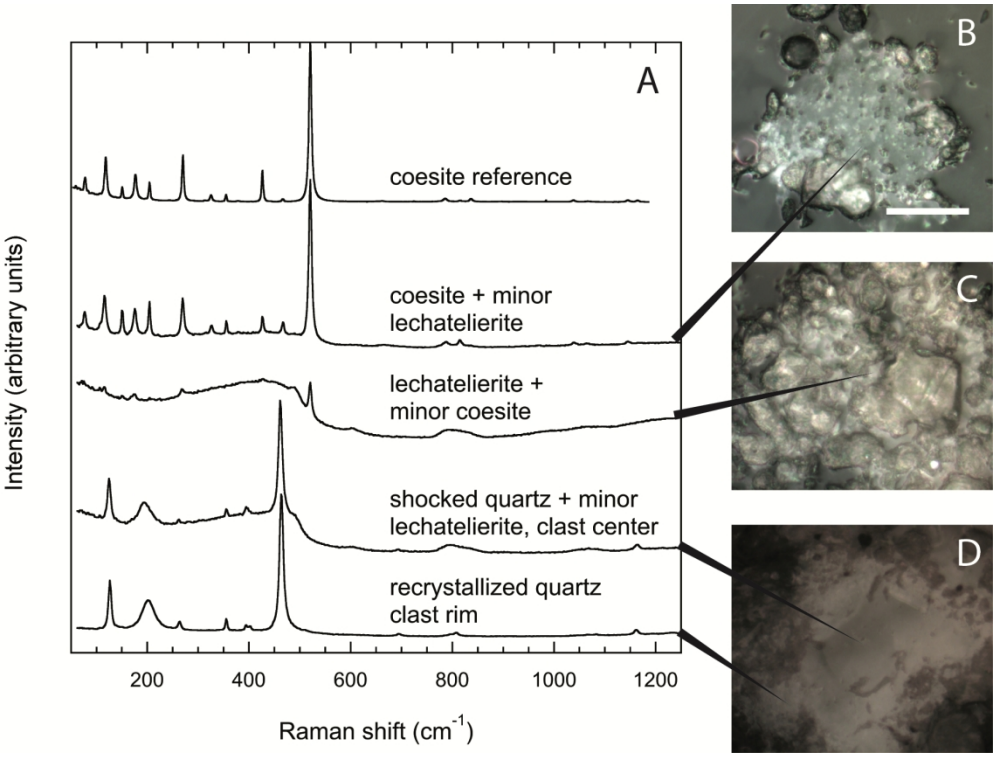

Fig.5: a) Typical Raman spectra of silica clasts in breccia P1. b) coesite-rich clast. Scale bar 20 microns. c) lechatelierite clast. d) quartz clast with homogeneous grey center and polycrystalline rims. Note the bad polishing on clast rims and on lechatelierite likely due to the mechanical contrast with the glassy matrix.

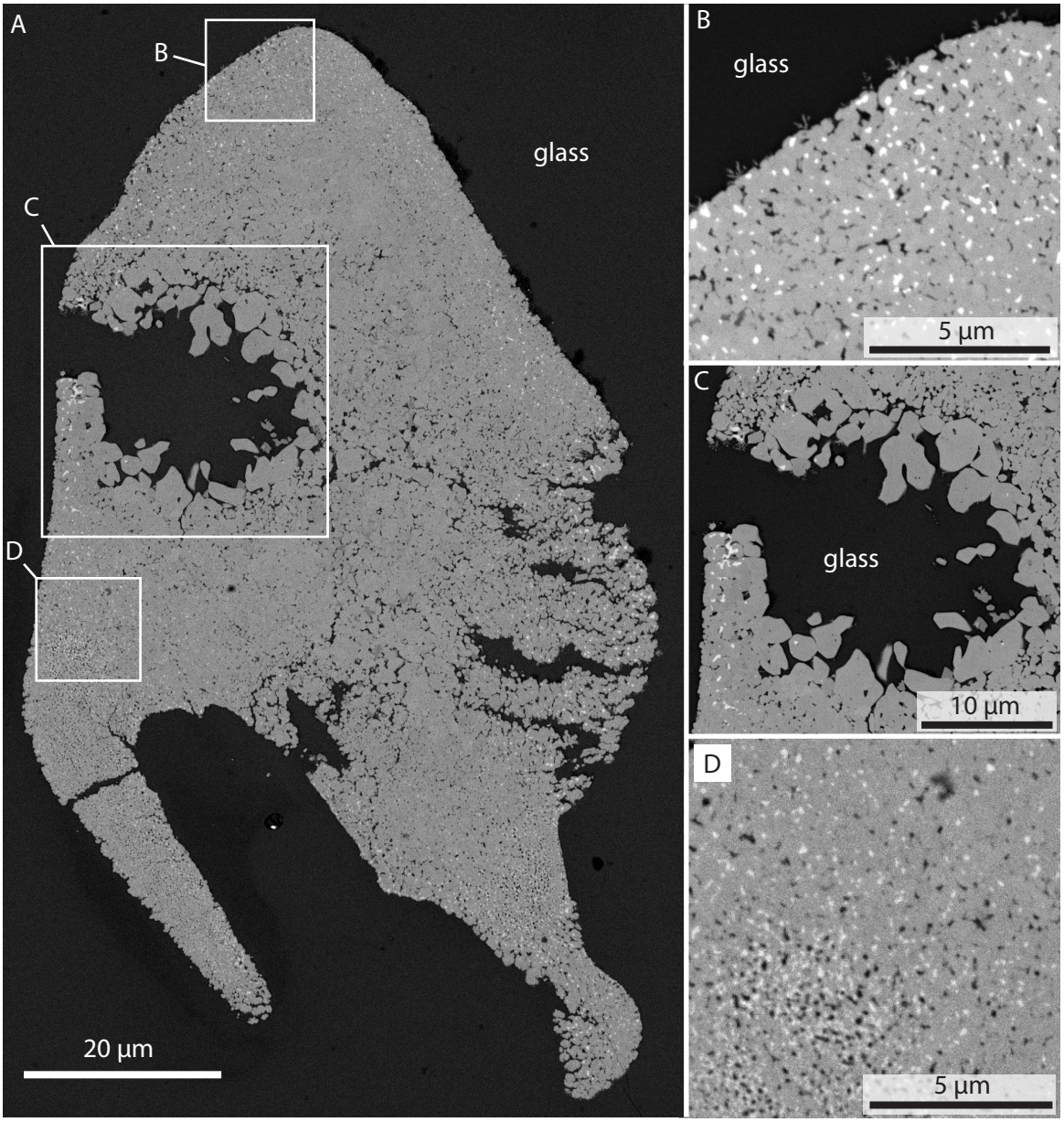
A
B
C
D
glass
20 µm
B
glass
5 µm
C
glass
10 µm
D
5 µm

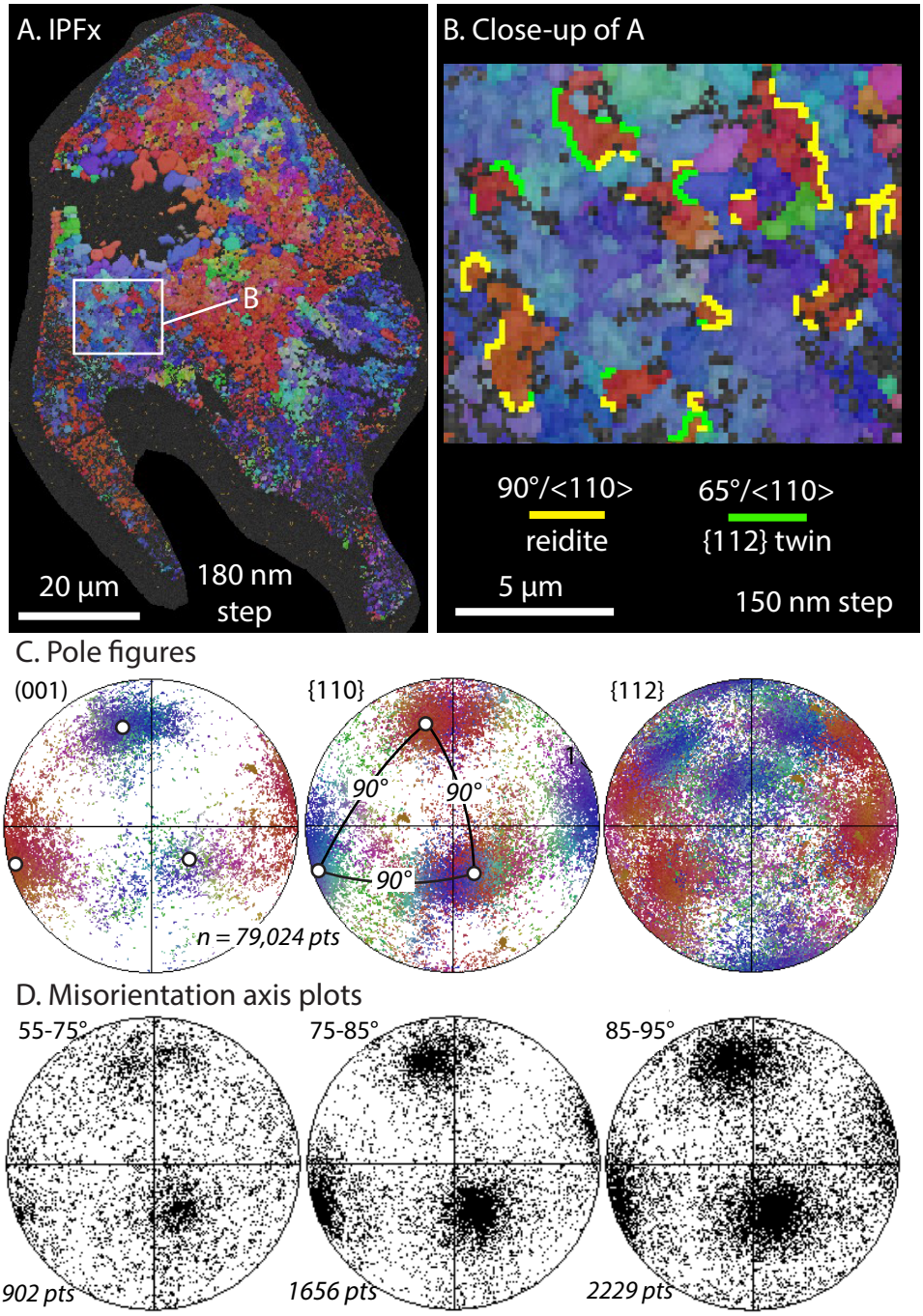
A. IPFx
B
20 µm
180 nm step
B. Close-up of A
90°/<110>
reidite
65°/<110>
{112} twin
5 µm
150 nm step
C. Pole figures
(001)
{110}
{112}
90°
90°
90°
n = 79,024 pts
D. Misorientation axis plots
55-75°
75-85°
85-95°
902 pts
1656 pts
2229 pts

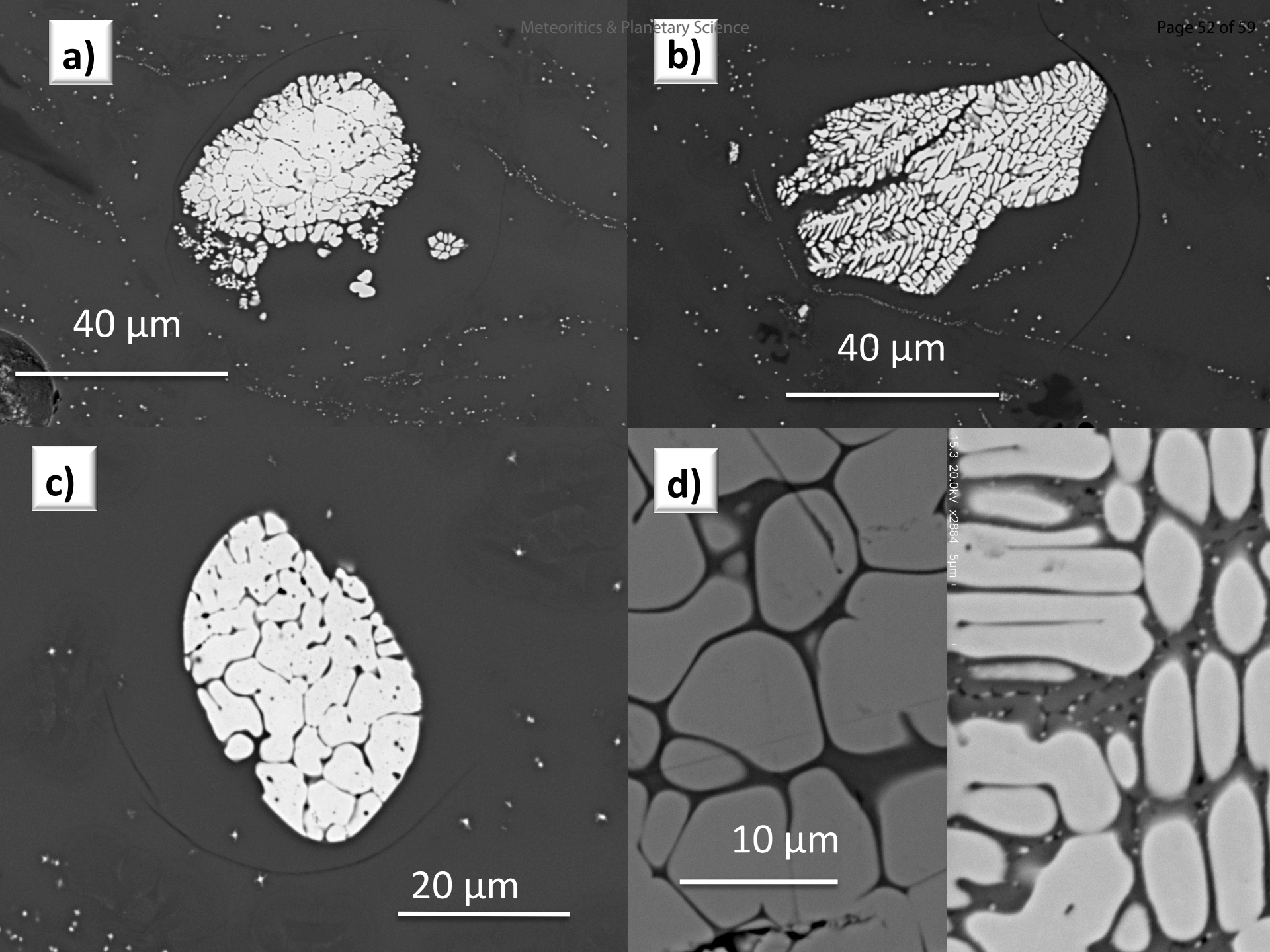
a)
40 µm
b)
40 µm
c)
20 µm
d)
10 µm
15.3 20.0kV x2984 5µm

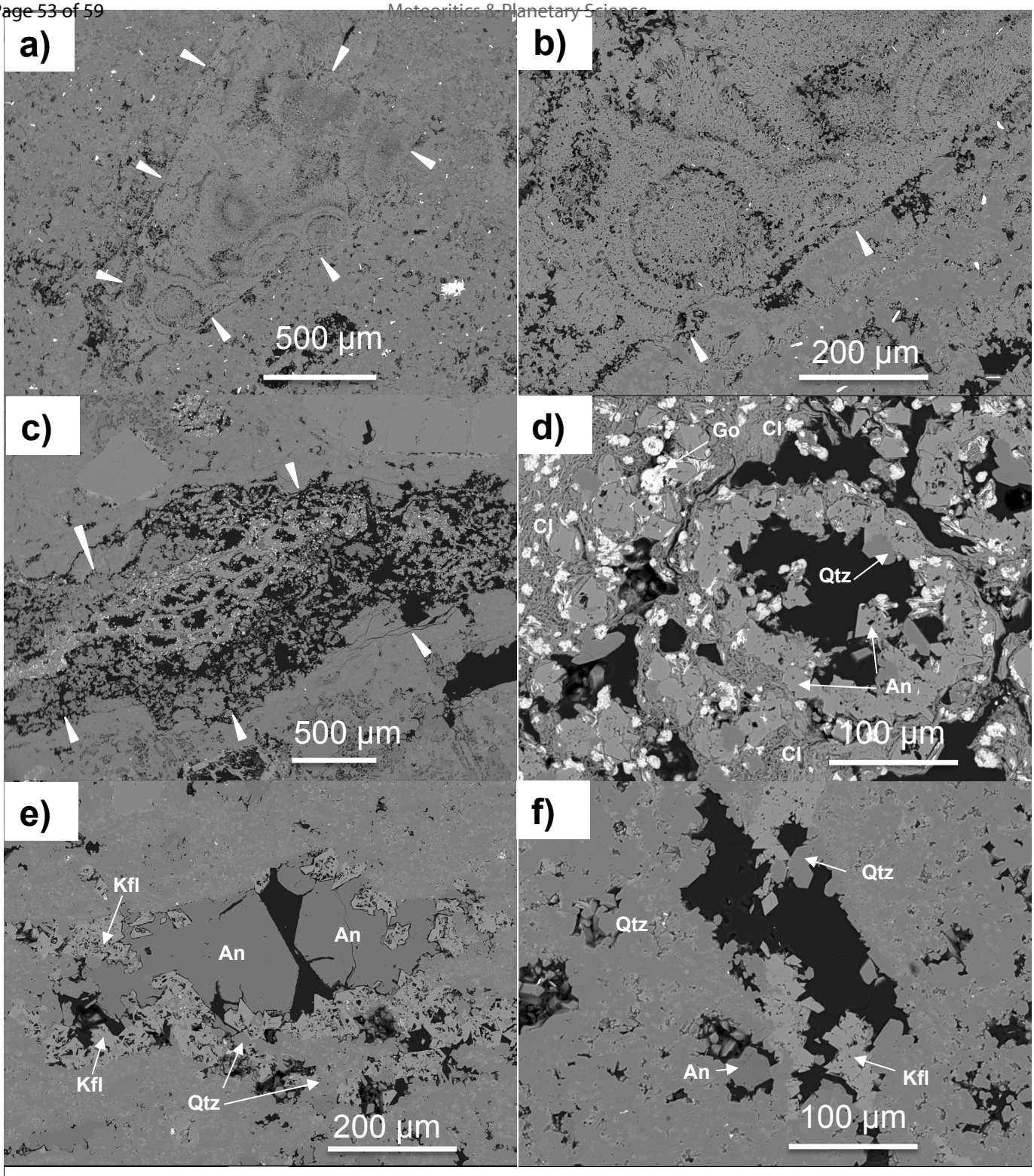
a)
500 µm
b)
200 µm
c)
500 µm
d)
Go
Cl
Cl
Qtz
An
Cl
100 µm
e)
Kfl
An
An
Kfl
Qtz
200 µm
f)
Qtz
Qtz
An
Kfl
100 µm

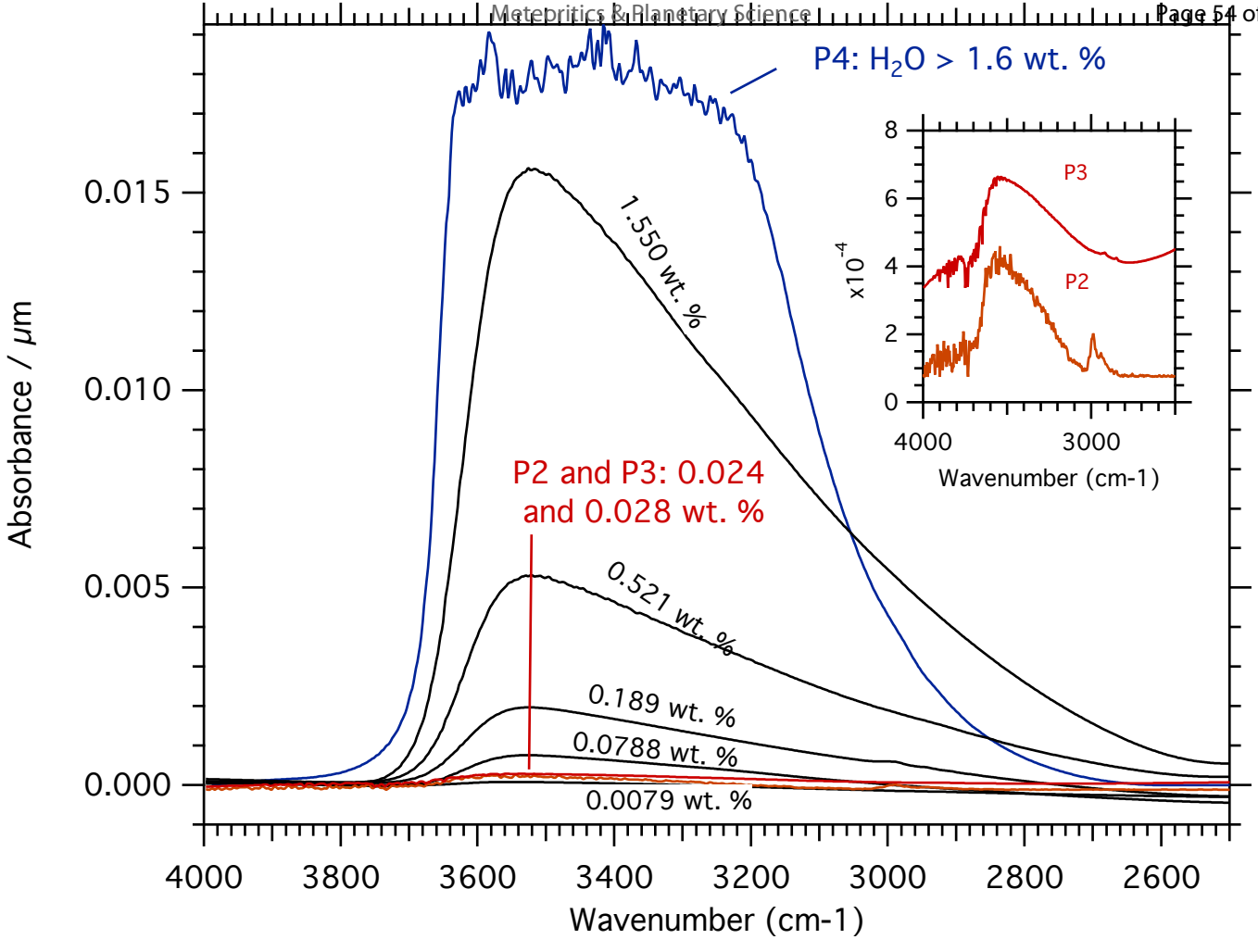
P4: H2O > 1.6 wt. %
1.550 wt. %
0.521 wt. %
0.189 wt. %
0.0788 wt. %
0.0079 wt. %
P2 and P3: 0.024
and 0.028 wt. %
P3
P2
x10-4
Absorbance / μm
Wavenumber (cm-1)
0.015
0.010
0.005
0.000
4000
3800
3600
3400
3200
3000
2800
2600
8
6
4
2
0

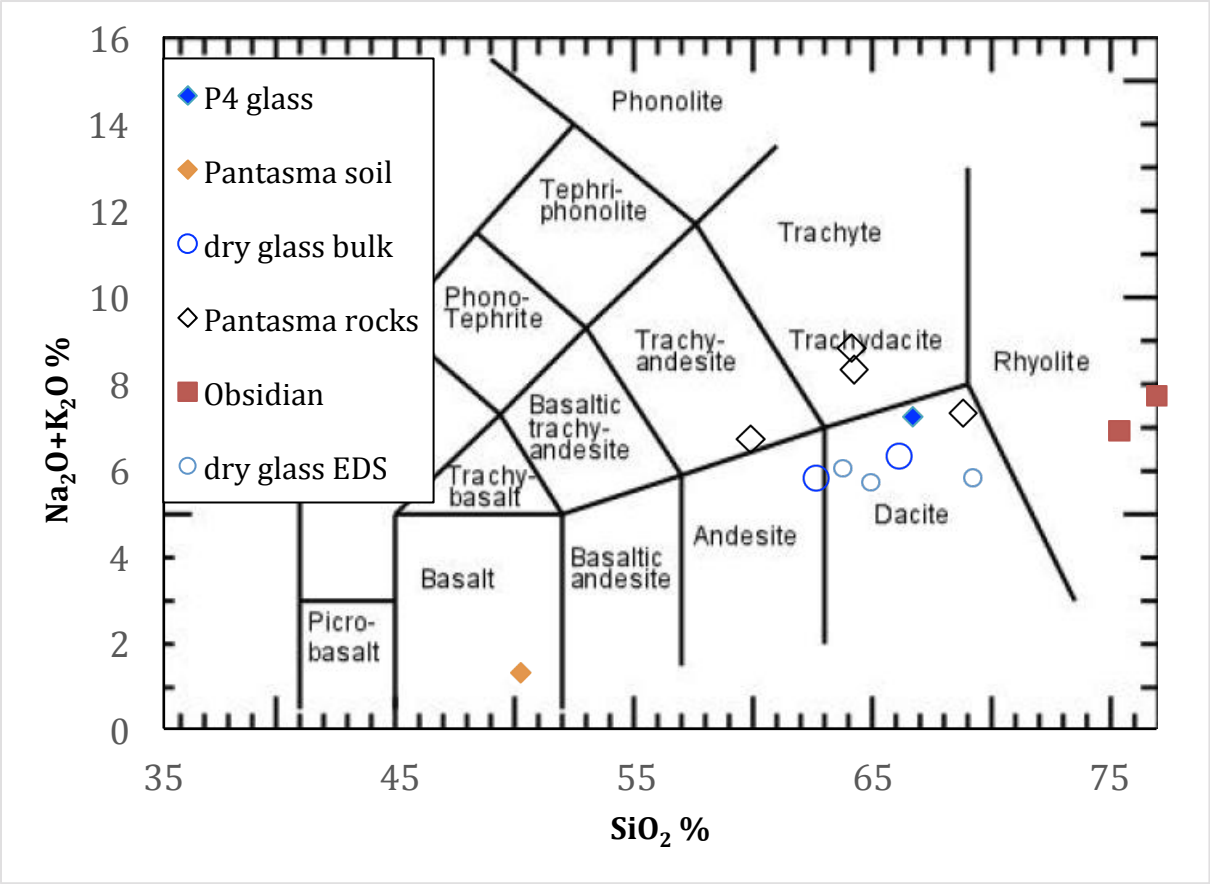
P4 glass
Pantasma soil
dry glass bulk
Pantasma rocks
Obsidian
dry glass EDS
Phonolite
Tephri-phonolite
Trachyte
Phono-Tephrite
Trachy-andesite
Trachydacite
Rhyolite
Basaltic trachy-andesite
Trachy-basalt
Andesite
Dacite
Basaltic andesite
Basalt
Picro-basalt
16
14
12
10
8
6
4
2
0
35
45
55
65
75
Na2O+K2O %
SiO2 %

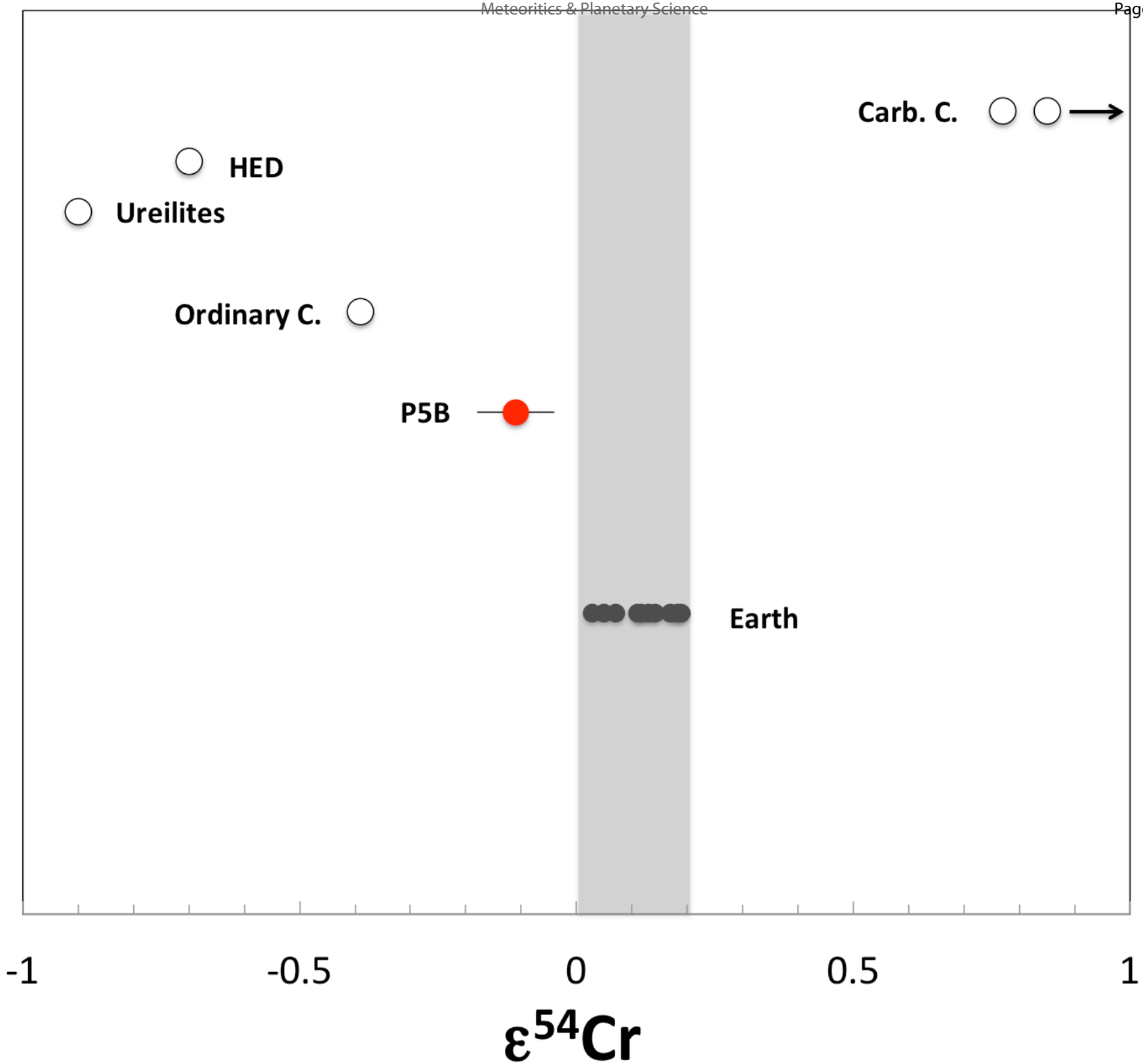
Carb. C.
HED
Ureilites
Ordinary C.
P5B
Earth
-1
-0.5
0
0.5
1
ε54Cr

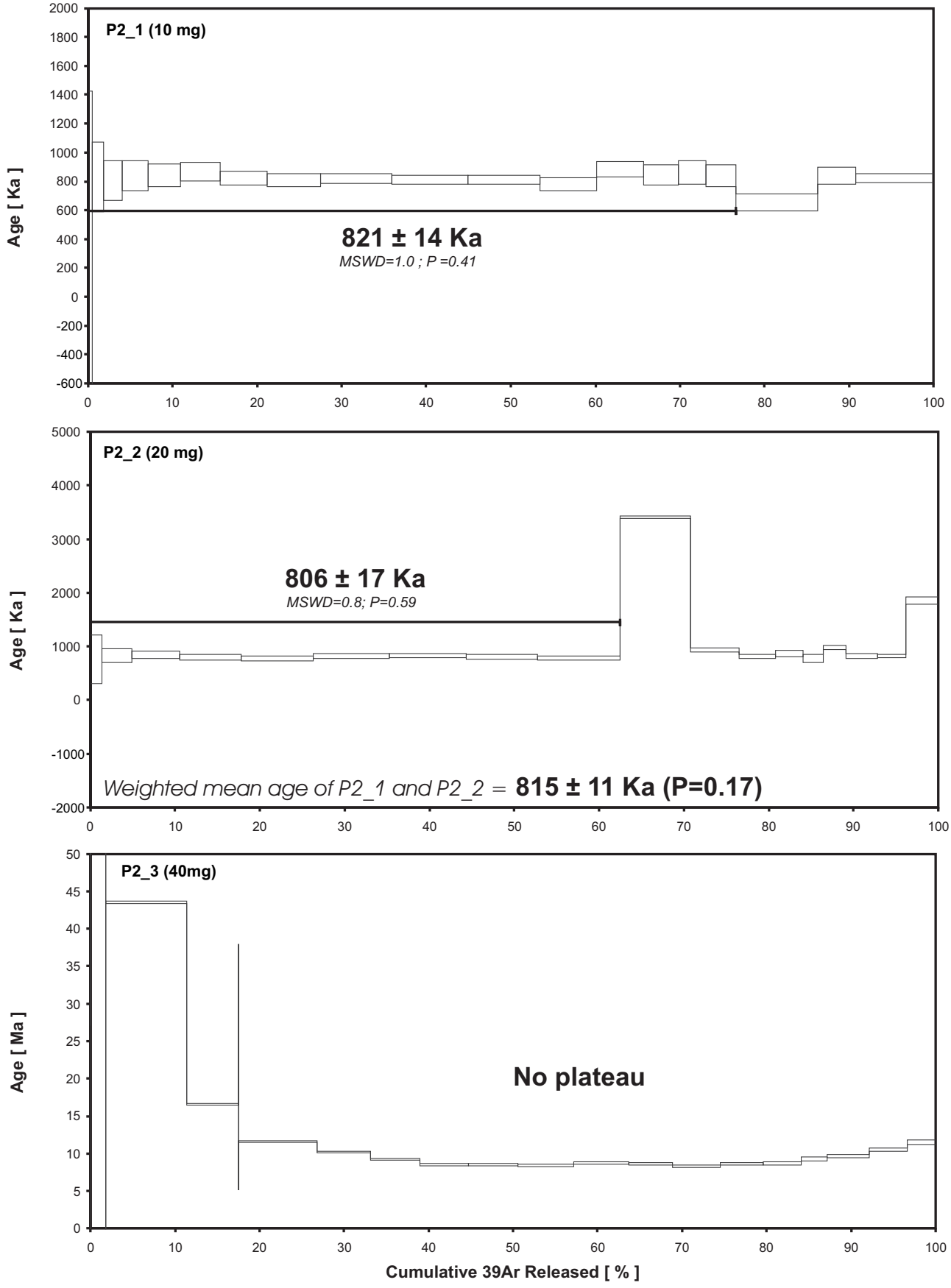
P2_1 (10 mg)
821 ± 14 Ka
MSWD=1.0 ; P =0.41
Age [Ka]
P2_2 (20 mg)
806 ± 17 Ka
MSWD=0.8; P=0.59
Weighted mean age of P2_1 and P2_2 = 815 ± 11 Ka (P=0.17)
Age [Ka]
P2_3 (40mg)
No plateau
Age [Ma]
Cumulative 39Ar Released [%]

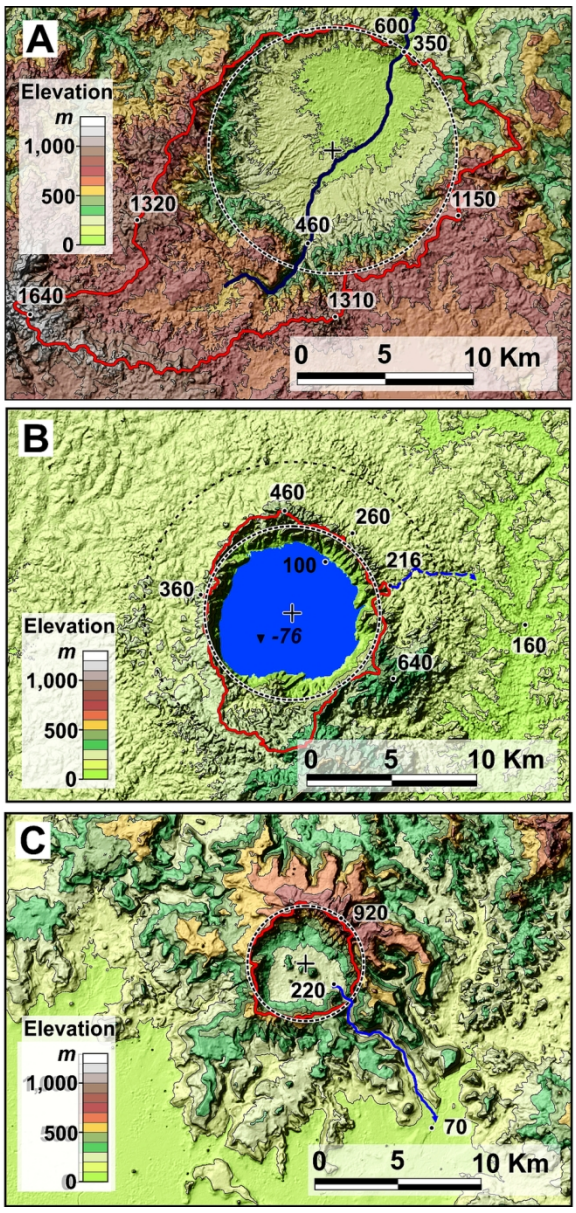

Fig. 14. Topographic maps of the Pantasma structure (a), Bosumtwi impact crater (b) and Las Lajas caldera (c). Contour line spacing: 100 m. Colour scale: elevation relative to the lowest point of each map. Numbers: elevation a.s.l. Red line: crater watershed. Blue line: outlet river (dashed: speculative past outlet). Dashed black lines: circles with diameters of 14.5, 10.5 and 6 km, centred (reticules) at W 85.948° N13.364°, W 85.727° N12.306°, and W 1.412° N 6.502 respectively.

80x164mm (300 x 300 DPI)

a)

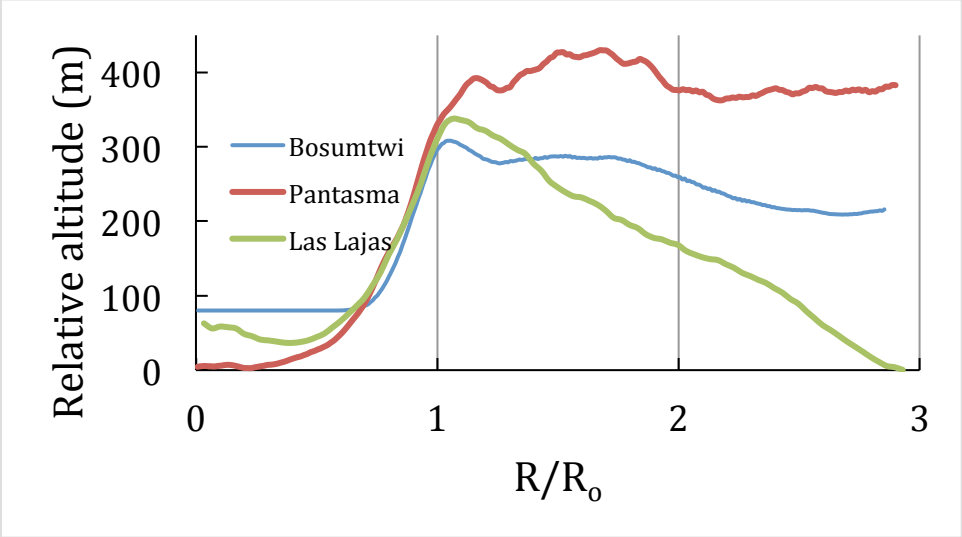
Relative altitude (m)
400
300
200
100
0
0
1
2
3
R/R$_o$
Bosumtwi
Pantasma
Las Lajas

b)

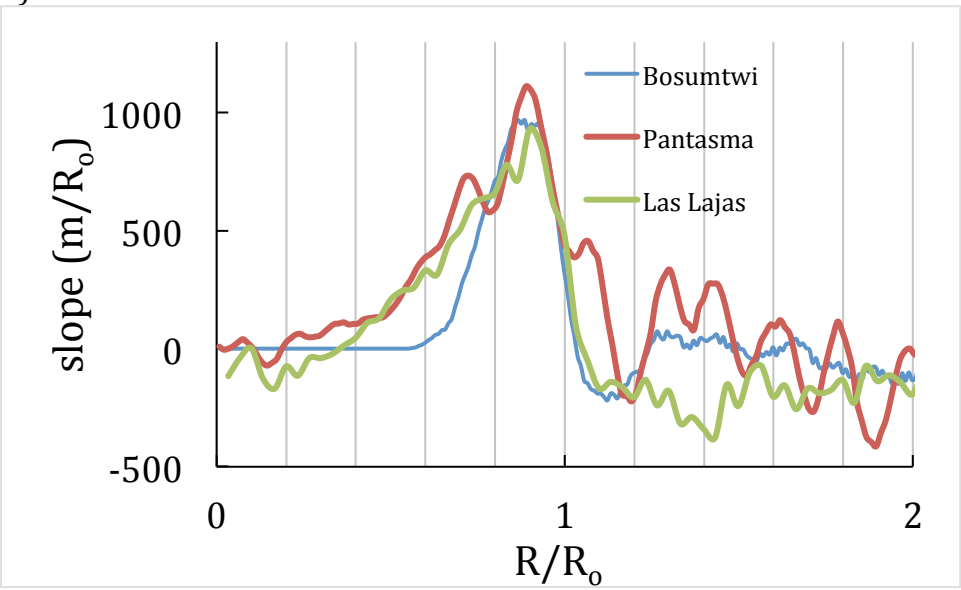
slope (m/R$_o$)
1000
500
0
-500
0
1
2
R/R$_o$
Bosumtwi
Pantasma
Las Lajas